ORIGINAL PAPER

Modeling and identification of a small fixed-wing UAV using estimated aerodynamic angles

Bogdan Løw-Hansen[1] · Richard Hann[1] · Kristoffer Gryte[1] · Tor Arne Johansen[1] · Christoph Deiler[2]

Abstract

This paper presents an experimental study on developing and validating a simulation-ready aerodynamic model for the Skywalker X8 unmanned aerial vehicle (UAV) using a hybrid output error method (OEM). Building on previous efforts, we introduce an updated 6-degree-of-freedom (DOF) nonlinear aerodynamic model and its linearized form. The key features of this work include the model's identification in the stability frame, achieved using estimated angle of attack and sideslip angle, and the use of a propulsion system model to obtained the motor speed data. The stability frame parameterization allows for direct comparisons with a larger set of UAV models and computational fluid dynamics (CFD) results, often presented in terms of lift and drag analysis. Key advancements include a residual distribution analysis that was successfully applied to identify and correct weaknesses in the initial drag and side force models. Additionally, the paper addresses the unique combination of challenges faced during this study and describes strategies for managing strong winds during experiments, use of a propulsion system model to obtain motor speed data, and utilization of estimated aerodynamic angles. The resulting model is validated against a separate set of maneuvers comprising 10-s-long sequences that include estimated body states, force and moment coefficients, and estimated air data states, (V_a, α, β), for both lateral and longitudinal maneuvers.

List of symbols

C_D, C_L	Drag and lift coefficients
$C_{\{l,m,n\}}$	Body-axis moment coefficients
C_T, C_Q	Propeller thrust and torque coefficients
$C_{\{X,Y,Z\}}$	Body-axis force coefficients
D	Propeller diameter (m)
F	Aircraft force vector (N)
I	Aircraft inertia matrix
I_b	Power supply current (A)
I_m, I_{m0}	Motor and zero load current (A)
I_p	Propeller moment of intertia (kg m^2)
$I_{\{x,y,z,xz\}}$	Aircraft moments of inertia (kg m^2)
J	Advance ratio
K_E	Back-emf constant (V/(rad/s))
M	Aircraft moment (Nm)
P_b	Power supply power (W)
P_{el}, P_m	Electrical and mechanical motor power (W)
Q	Propeller torque (Nm)
Q_m	Motor torque (Nm)
R	SO(3) rotation matrix
R	Motor resistance (Omega)
S	Wing area (m^2)
T	Propeller thrust (N)
U	Motor voltage (V)
U_b	Power supply voltage (V)
V_a	Airspeed (m/s)
a_x, a_y, a_z	Body-axis linear accelerations (m/s^2)
b	Wingspan (m)

✉ Bogdan Løw-Hansen
    bogdan.l.hansen@ntnu.no

✉ Richard Hann
    richard.hann@ntnu.no

    Kristoffer Gryte
    kristoffer.gryte@ntnu.no

    Tor Arne Johansen
    tor.arne.johansen@ntnu.no

    Christoph Deiler
    christoph.deiler@dlr.de

1   Department of Engineering Cybernetics, Norwegian University of Science and Technology, NTNU, 7491 Trondheim, Norway

2   German Aerospace Center (DLR), 38108 Braunschweig, Germany

$\bar{c}$	Mean aerodynamic chord (m)
$\boldsymbol{f}$	Specific force vector (m/s^2)
g	Gravitiational acceleration (m/s^2)
h	Altitude (m)
$\boldsymbol{h}_p$	Propeller angular momentum (kg m^2/s)
m	Aircraft mass (kg)
$\boldsymbol{p}$	Position vector (m)
p, q, r	Body-axis angular velocities (rad/s)
p^*, q^*, r^*	Nondimensional angular velocitites
$\bar{q}$	Dynamic pressure (Pa)
$\boldsymbol{r}$	Distance vector (m)
u, v, w	Body-axis linear velocities (m/s)
u_a, v_a, w_a	Aerodynamic system velocities (m/s)
$\boldsymbol{v}$	Linear velocity vector (m/s)
x, y, z	Body-axis position coordinates (m)
Ω_p	Rotational motor speed (rad /s)
α	Angle of attack (rad)
β	Sideslip (rad)
γ	Flight path angle (rad)
δ_a, δ_e	Aileron and elevator deflection (rad)
δ_{el}, δ_{er}	Left and right elevon deflections (rad)
δ_r	Rudder deflection (rad)
δ_t	Throttle command normalized $\in [0,1]$
ρ	Air density (kg/m^3)
ϕ, θ, ψ	Roll, pitch, yaw angles (rad)
$\boldsymbol{\omega}$	Angular rate vector (rad/s)
{b}	Body frame
{i}	Inertial frame
{m_I}	Sensor frame
{n}	North-East-Down (NED) frame
{s}	Stability frame
{w}	Wind frame
$_a$	Relative velocity subscript
$_w$	Wind velocity subscript
$\hat{}$	Hat indicates model prediction results

Abbreviations

CFD	Computational fluid dynamics
CG	Center of gravity
DOF	Degree-of-freedom
EE	Equation error
EKF	Extended Kalman filter
GNC	Guidance, navigation, and control
GNSS	Global navigation satellite system
IMU	Inertial measurement unit
NED	North-East-Down
OE	Output error
OEM	Output error method
RPAS	Remotely piloted aircraft system
UAS	Uncrewed aircraft system
UAV	Unmanned aerial vehicle

1 Introduction

It is clear that by 2024, small, cost-effective unmanned aerial vehicles (UAVs) [also uncrewed aircraft systems (UASs), remotely piloted aircraft systems (RPASs), or simply drones], have transcended their niche hobby and research applications to become an integral part of various industry and defense sectors [1, 2]. Although professional users find these platforms robust enough for many of their applications, the increased use has revealed many limitations related to the operation of small UAVs in real-world scenarios; among the most challenging issues concern operations in harsh weather conditions [3, 4]. One way to approach these challenges is through simulation-based testing and development. A high-fidelity model and a simulator framework make it possible to test and develop guidance, navigation, and control (GNC) algorithms capable of handling various adverse weather conditions without risking losing the aircraft, while it is in the air. Motivated by our own research into performance-based aircraft monitoring and operation in icing conditions [5–7], we aim to facilitate this simulation-based approach by presenting the model development process and the identified model parameters of the Skywalker X8 UAV. The UAV is a flying wing with a wingspan of 2.1 m controlled by two elevons and a rear-mounted propeller, as shown in Fig. 1. The physical properties of the aircraft are shown in Table 1.

1.1 Review of existing models

Previous efforts on the modeling of the Skywalker X8 UAV include [8], which focused on identifying static aerodynamic coefficients based on wind tunnel experiments, and [9], which extended these results through system identification experiments to identify velocity-based parameters. Although the velocity-based model in [9] provides valuable information on aircraft dynamics, it is not easily comparable to most other models available in the literature. There

Fig. 1 Skywalker X8 UAV

Table 1 Physical properties of the Skywalker X8 UAV

Property	Value
m	3.364 kg
I_x	0.325 kg m^2
I_y	0.140 kg m^2
I_z	0.400 kg m^2
I_{xz}	0.029 kg m^2
$\bar{c}$	0.36 m
b	2.10 m
S	0.75 m^2

are two main reasons for this: first, the model in [9] has a complex structure with a high number of parameters and nonlinear regressors; second, the model is identified in the body frame, as opposed to the stability frame used in the classical system identification approaches [10, 11]. Furthermore, the model coefficients identified in the stability frame are more convenient to compare against the results based on computational fluid dynamics (CFD), which are presented primarily in terms of the lift and drag curves. This is particularly relevant in the case of aircraft icing research, where a considerable amount of data has been accumulated

on the change in lift and drag coefficients as a function of ice accretion [12–18]. Consequently, to allow for convenient validation and comparison with available research, the aerodynamic model presented in this paper was identified in the stability frame. The system identification process was performed following the classical time-domain methodology described in [10, 11], which was greatly simplified by the access to the DLR's (German Aerospace Center) system identification tool Fitlab [19].

In the past decade, several research groups have successfully conducted system identification of aerodynamic models for small fixed-wing UAVs; an overview of the most recent results is presented in Table 2. A clear takeaway from the presented overview is that most of the identified models are parameterized in the body frame. One of the reasons for this is the lack of direct measurements of the angle of attack and sideslip on low-cost UAV platforms. Identifying a model in the stability frame would therefore require the use of estimated states, which is done in this paper. Although it introduced the state estimation error into the identification process, a model described in terms of lift and drag coefficients is necessary in certain applications such as UAV-icing, where most of the available research on aerodynamic

Table 2 Overview of recently published small fixed-wing UAV models identified using flight experiments

Paper	Year	Platform	Speed (m/s)	Mass (kg)	Wingspan (m)
Arifianto et al. [20]	2015	Telemaster	16	3.2	1.8
Grymin et al. [21]	2016				
Reinhardt et al. [9]	2022	Skywalker X8	18	3.4	2.1
Lu et al. [22]	2018	Hangar 9 PA-18 Super Cub	18	7.5	2.7
Simmons et al. [23]	2019	HobbyKing Bix3	12	1.2	1.5
Simmons et al. [24]	2023	CZ-150	24	4.8	2.1
Dorobantu et al. [25]	2013	Ultra Stick 25e	19	2.0	1.3
Venkataraman et al. [26]	2019	Sentera Vireo	19	1.3	1.0
Matt et al. [27]	2022	KHawk Zephyr3-R	17	2.2	1.2
Matt et al. [28]	2023				

Paper	Method and domain	Explanatory variables	Identified coefficients
Arifianto et al. [20]	OE time	$\alpha, \beta, p, q, r, \delta_e, \delta_a, \delta_r$	$C_X, C_Y, C_Z, C_l, C_\mathrm{m}, C_n$
Grymin et al. [21]	EE time	$\alpha, \beta, p, q, r, \delta_e, \delta_a, \delta_r, \delta_\mathrm{t}, C_\mathrm{T}$	$C_X, C_Y, C_Z, C_l, C_\mathrm{m}, C_n$
Reinhardt et al. [9]	OE time	$u, v, w, p, q, r, \delta_e, \delta_a, \delta_\mathrm{t}$	X, Y, Z, L, M, N[a]
Lu et al. [22]	OKID[c] time	$\alpha, \beta, p, q, r, \delta_e, \delta_a, \delta_r, \delta_\mathrm{t}$[c]	State space models[a]
Simmons et al. [23]	OE time	$u, v, w, p, q, r, \delta_e, \delta_a, \delta_r$	$C_X, C_Y, C_Z, C_l, C_\mathrm{m}, C_n$
Simmons et al. [24]	EE time	$\alpha, \beta, p, q, r, \delta_e, \delta_a, \delta_r, J^{-1}$	$C_X, C_Y, C_Z, C_l, C_\mathrm{m}, C_n$
Dorobantu et al. [25]	OE frequency	$u, v, w, p, q, r, \delta_e, \delta_a, \delta_r$	State space models[a]
Venkataraman et al. [26]	OE frequency	$u, v, w, p, q, r, \phi, \theta, \delta_e, \delta_a, \delta_r$	State space models[a]
Matt et al. [27]	OE frequency	$u, v, w, p, q, r, \phi, \theta, \delta_e, \delta_a$	$C_D, C_Y, C_L, C_l, C_\mathrm{m}, C_n$[b]
Matt et al. [28]	OE frequency	$u, w, q, \theta, \delta_e, \Omega_\mathrm{p}$	C_D, C_L, C_m[b]

[a]Generalized force and moment coefficients. X, Y, Z, L, M, N notation is not used outside the table

[b]The stability frame coefficients are computed from the generalized force and moment coefficients identified in the form of state-space models

[c]Observer/Kalman Filter Identification (OKID), the explanatory variables were not mentioned explicitly but are based on derivation in [29]

performance penalties is described as the change in lift and drag. On the technical level, the main difference between the approaches in Table 2 lies in the choice between the time- or frequency-domain signals, and second in the use of the equation error (EE) or the output error (OE) method for the definition of the objective function error. These choices are often dependent on the available software tools, model complexity, and engineering preferences such as model accuracy metrics.

The papers in Table 2 provide a substantial variety in identified platforms. However, variations in modeling assumptions and use-case-specific adaptations do not always align with user-specific requirements. This paper aims to address this challenge by contributing to the set of validated small fixed-wing UAV models parameterized in the stability frame coefficients, thus offering users a wider selection to better match their specific application requirements.

In summary, this paper presents a detailed tutorial on the modeling and identification of a simulation-ready 6-degree-of-freedom (DOF) aerodynamic model based on the Skywalker X8 UAV platform. To our best knowledge, it is the first paper to address the unique combination of challenges posed by: model identification in the stability frame using estimated values of aerodynamic angles, estimation of motor speed from a propulsion system model, and the use of data obtained in windy conditions. The final nonlinear model comprises 44 coefficients distributed among the aerodynamic, propulsion, and servo models. The presentation and analysis of the model prediction results are done with the primary objective of enabling high-fidelity simulation testing using the identified models.

2 Methods

This section includes the theory necessary to set up and perform system identification based on the time-domain output error method (OEM) [10, Chap. 6.2]. More specifically, this concerns the transformation of sensor measurements from sensor frame to center of gravity (CG), propulsion force and moment calculations, aerodynamic system modeling, and simulation. The theory related to the optimization solver used by the OEM is considered to be outside of the scope of this paper and is therefore not included; if necessary, the relevant information can be found in [11, 19].

There are many ways to express vectors and rotations. In this paper, the notation from [30] is adopted. An example of vectors and a rotation between the body frame {b} and North-East-Down (NED) frame {n} is presented here, where the NED frame is considered inertial:

$\boldsymbol{v}_{nb}^{b}$—Linear velocity vector of the body frame origin relative to the NED origin, expressed in {b},

$\boldsymbol{v}_{nb}^{n}$—Linear velocity vector of the body frame origin relative to the NED origin, expressed in {n},

$\boldsymbol{\omega}_{nb}^{b}$—Angular velocity vector of {b} relative to {n}, expressed in {b},

$\boldsymbol{R}_{b}^{n}$—SO(3) rotation matrix that transforms a vector from {b} to {n}.

2.1 Sensor measurement transformations

When working with aircraft dynamics and kinematics, the time derivative of a vector in a rotating reference frame must be defined. In (1, let $^{i}\mathrm{d}/\,\mathrm{d}t$ denote the time differentiation in the inertial frame {i}, and $^{b}\mathrm{d}/\,\mathrm{d}t$ in the body frame {b}. The time derivative of a vector $\vec{(\cdot)}$ in a rotating reference frame {b}, expressed in the body frame {b}, has two parts: a part that accounts for the rate of change of the vector in the rotating reference frame {b} and a part that accounts for the rotation of the axis of the reference frame {b} in the inertial frame {i}, denoted by $\boldsymbol{\omega}_{ib}^{b}$ [30, Chap. 3.1]

$$\frac{^{i}\mathrm{d}}{\mathrm{d}t}\vec{(\cdot)} = \frac{^{b}\mathrm{d}}{\mathrm{d}t}\vec{(\cdot)} + \boldsymbol{\omega}_{ib}^{b} \times \vec{(\cdot)}. \tag{1}$$

Moreover, the location of the origin of the body frame with respect to the aerodynamic center and the CG has to be defined. For Skywalker X8, the origin of the body frame {b} is placed in the aerodynamic center that is assumed to coincide with the nominal CG of UAV, so that the vector from the origin of {b} to CG in the body frame is $\boldsymbol{r}_{bCG}^{b} = [0, 0, 0]^{\top}$. This simplifying assumption is reasonable when the CG is not expected to change during flight and the distance between the aerodynamic center and CG is small. Depending on the UAV, the aerodynamic center and CG could be far apart. The validity of the assumption must therefore be assessed separately for each platform. Otherwise, the location of the aerodynamic center with respect to CG must be taken into account when computing the aerodynamic moments, as shown in [11, Eq. (6.75)].

In a moving vehicle, measurements of acceleration and estimates of linear velocity change based on the location of the sensors in the vehicle. Therefore, it is necessary to transform the inertial measurements from the sensor frame {m_I} to the aircraft CG to obtain the correct reading of the movement of the aircraft. The transformation can be performed on the basis of the distance vector that specifies the location of the sensor frame {m_I} with respect to CG

$$\boldsymbol{r}_{m_I CG}^{b} = \boldsymbol{r}_{bCG}^{b} - \boldsymbol{r}_{bm_I}^{b} = \begin{bmatrix} x_{CG} - x_{m_I} \\ y_{CG} - y_{m_I} \\ z_{CG} - z_{m_I} \end{bmatrix}. \tag{2}$$

The velocities in the flight experiment data $\boldsymbol{v}_{nm_I}^{b}$ are the output of an extended Kalman filter (EKF) located in the sensor frame and therefore must be transformed from the sensor

frame to CG. Following [30, Chap. 14], the transformation can be performed in the following way:

$$v_{nb}^b = v_{nm_I}^b + \omega_{nb}^b \times r_{m_I CG}^b \quad , \quad v_{nb}^b = \begin{bmatrix} u \\ v \\ w \end{bmatrix} \quad , \quad \omega_{nb}^b = \begin{bmatrix} p \\ q \\ r \end{bmatrix}. \tag{3}$$

Similarly, the accelerations measured by the inertial measurement unit (IMU) in the sensor frame $f_{nm_I}^b$ must be transformed to CG. The transformation is derived by the time differentiation of (3 assuming that $\dot{r}_{m_I CG}^b = 0$ and recognizing that $v_{nm_I}^b$ is an inertial vector, which can be directly differentiated

$$f_{nb}^b = f_{nm_I}^b + \dot{\omega}_{nb}^b \times r_{m_I CG}^b + \omega_{nb}^b \times (\omega_{nb}^b \times r_{m_I CG}^b). \tag{4}$$

2.2 Propulsion system modeling

The Skywalker X8 UAV is driven by a pusher propeller located behind the fuselage. When the propeller rotates, it generates a thrust, which pushes the UAV forward, and a roll moment, which the motor must match to sustain the desired motor speed. Additionally, the propeller generates a gyroscopic moment which resists deviation from its rotation axis. The generated roll moment is mainly due to drag and friction associated with propeller rotation, while the gyroscopic moment is caused by the rotating mass of the propeller and the motor shaft. The modeling of the drag-related roll moment is described in [31, Chap. 4.3], while the gyroscopic effect model can be found in [10, Chap. 3.2]. In general, the gyroscopic effect is often neglected, as it is an order of magnitude smaller than the total torque, although it can become significant when the rotating mass is large enough. The propeller torque model should therefore be based on available data and model requirements.

The propeller thrust T and torque Q in Eqs. (6) and (7) are modeled as functions of the airspeed V_a, the motor speed Ω_p, and the advance ratio J defined in (5). The effects of the Reynolds number and the Mach number are omitted as they are not as significant at slow speeds [32–34], which constitute the envelope of interest for small fixed-wing UAVs

$$J = \frac{2\pi V_a}{\Omega_p D} \tag{5}$$

$$Q = \frac{\rho D^5}{4\pi^2} C_Q(J)\Omega_p^2 \tag{6}$$

$$T = \frac{\rho D^4}{4\pi^2} C_T(J)\Omega_p^2. \tag{7}$$

In this study, as indicated by the modeling results in Sect. 3, the torque and thrust coefficients C_Q and C_T are represented as second- and third-order polynomials of J, respectively

$$C_Q(J) = C_{Q0} + C_{Q1} \cdot J + C_{Q2} \cdot J^2 \tag{8}$$

$$C_T(J) = C_{T0} + C_{T1} \cdot J + C_{T2} \cdot J^2 + C_{T3} \cdot J^3. \tag{9}$$

The gyroscopic propeller torque, $M_{prop,gyro}^b$, generated by the rotating mass of the propeller in the body axis, is determined by the derivative of the propeller's angular momentum h_p. This angular momentum is a function of the propeller's inertia I_p, and its rotational speed Ω_p

$$h_p = \begin{bmatrix} I_p\Omega_p \\ 0 \\ 0 \end{bmatrix}. \tag{10}$$

The reference frame in which the torque is applied is rotating relative to the inertial frame. The gyroscopic propeller torque is therefore defined according to (1, verified in [10, Chap. 3.2]

$$M_{prop,gyro}^b = \dot{h}_p + \omega_{nb}^b \times h_p = \begin{bmatrix} I_p\dot{\Omega}_p \\ 0 \\ 0 \end{bmatrix} + \begin{bmatrix} 0 \\ I_p\Omega_p r \\ -I_p\Omega_p q \end{bmatrix} = \begin{bmatrix} I_p\dot{\Omega}_p \\ I_p\Omega_p r \\ -I_p\Omega_p q \end{bmatrix}. \tag{11}$$

Combining the aerodynamic drag and friction torque in (6 with the gyroscopic torque in (11 results in the following propeller torque model:

$$M_{prop} = \begin{bmatrix} Q \\ 0 \\ 0 \end{bmatrix} + M_{prop,gyro}^b. \tag{12}$$

The sign of the torque produced depends on the direction of rotation and the location of the propeller with respect to CG. For a clockwise rotating propeller mounted at the front of the aircraft along the aircraft's x-axis, the produced torque is positive w.r.t. body-fixed axes. For a rear-mounted propeller, as in the Skywalker X8 UAV, the torque produced by the propeller is negative, leading to the following definition:

$$M_{prop,rear} = -M_{prop}. \tag{13}$$

2.3 Aerodynamic modeling and simulation

This section presents the equations of motion and other relevant relations needed to simulate the UAV dynamics and reproduce the measured flight data.

2.3.1 Flying wing configuration

The aerodynamic modeling of an aircraft is highly affected by its geometry and control surface configuration. The Skywalker X8 UAV is a flying wing platform with two control surfaces—right and left elevons (δ_{er}, δ_{el}), normally specified in radians. In this configuration, the elevons replace the function of the elevator and the aileron (δ_e, δ_a), which are the standard control inputs used in aerodynamic modeling. Driving the elevons together emulates the elevator command, while driving them differentially emulates the aileron command. Mathematically, the transformation from elevons to elevators and ailerons is defined as follows:

$$\begin{bmatrix} \delta_e \\ \delta_a \end{bmatrix} = \frac{1}{2} \begin{bmatrix} 1 & 1 \\ -1 & 1 \end{bmatrix} \begin{bmatrix} \delta_{er} \\ \delta_{el} \end{bmatrix}. \tag{14}$$

Furthermore, the platform has no rudder, so the rudder input δ_r is not used. Instead, the Skywalker X8 has blended winglets to provide directional stability, as seen in Fig. 1. The propulsion on the Skywalker X8 platform is achieved through a single rear-mounted propeller, controlled by a throttle input $\delta_t \in [0, 1]$.

2.3.2 Modeling aerodynamic forces and moments

Modeling and dynamic system simulation are crucial components of the output-error-based system identification method. More specifically, OEM requires computation of the system dynamics based on a set of model parameters that can be updated iteratively during the identification process. In this way, the model parameters can be adjusted to minimize the discrepancy between the simulated model output and the measured experiment data.

The calculation of aerodynamic forces and moments starts with the aerodynamic state of the aircraft, i.e., the airspeed V_a, the angle of attack α, and the sideslip angle β. The aerodynamic state can be derived from the inertial and wind velocities as shown in Eqs. (15) and (16)

$$\begin{bmatrix} u_a \\ v_a \\ w_a \end{bmatrix} = \begin{bmatrix} u - u_w \\ v - v_w \\ w - w_w \end{bmatrix} \tag{15}$$

$$V_a = \sqrt{u_a^2 + v_a^2 + w_a^2} \quad , \quad \alpha = \tan^{-1}\left(\frac{w_a}{u_a}\right) \quad , \quad \beta = \sin^{-1}\left(\frac{v_a}{V_a}\right). \tag{16}$$

Given the aerodynamic state of the aircraft, the forces and moments generated can be computed. The exact relation depends on the structure of the model, normally given as a set of polynomial equations [10]. The selection of the model structure is part of the system identification process. In this study, the selection was initially based on previous modeling results for similar UAV platforms [23, 24, 28] and then verified using the stepwise regression algorithm described in [10, Chap. 5]. Following the convention in [10, Chap. 5], the resulting aerodynamic model structure is defined with stability frame force coefficients and body frame moment coefficients.

Although the actual drag is generated in the wind frame, decomposing the wind frame drag into the side force and drag in the stability frame would introduce coupling between the longitudinal and lateral dynamics. To keep the model and the identification process less complex, this specific coupling is assumed to be negligible and is omitted in this model, resulting in the following set of equations:

$$C_L = C_{L0} + C_{L\alpha}\alpha + C_{Lq}q^* + C_{L\delta e}\delta_e \tag{17a}$$

$$C_D = C_{D0} + C_{Dq}q^* + C_{DCT}C_T + C_{Dk1}C_L + C_{Dk2}C_L^2 \tag{17b}$$

$$C_m = C_{m0} + C_{m\alpha}\alpha + C_{mq}q^* + C_{m\delta e}\delta_e \tag{17c}$$

$$C_Y = C_{Y0} + C_{Y_\beta}\beta + C_{Yp}p^* + C_{Yr}r^* + C_{Y\delta a}\delta_a \tag{18a}$$

$$C_l = C_{l0} + C_{l_\beta}\beta + C_{lp}p^* + C_{lr}r^* + C_{l\delta a}\delta_a \tag{18b}$$

$$C_n = C_{n0} + C_{n_\beta}\beta + C_{np}p^* + C_{nr}r^* + C_{n\delta a}\delta_a, \tag{18c}$$

where $\delta_e, \delta_a, \delta_t$ are the elevator, aileron, and throttle control commands and $[p^*, q^*, r^*]$ are the nondimensional angular rates normalized by airspeed and wing size, i.e., the wingspan b and the mean aerodynamic chord length $\bar{c}$

$$p^* = \frac{pb}{2V_a} \quad , \quad q^* = \frac{q\bar{c}}{2V_a} \quad , \quad r^* = \frac{rb}{2V_a}.$$

Due to its low weight and large surface area, the Skywalker X8 UAV is highly susceptible to wind gusts. During the flight experiments, the UAV encountered strong winds, which impacted the overall quality of the measured data. Consequently, to ensure that the model does not overfit the data, a low model complexity and compatibility with similar research were weighted to a greater degree in the modeling process. The aerodynamic model in Eqs. (17) and (18) is almost linear, except for the drag equation, where the nonlinearities are introduced in thrust and lift regressors. Moreover, the model is decoupled along the longitudinal–lateral axes. Although actual dynamics are likely coupled, and the stepwise regression results suggested that sideslip explains some of the variations in lift and drag, including sideslip in the longitudinal model did not improve the overall model prediction error.

2.3.3 Stability to body frame transformation

The lift and drag forces in (17 are generated in the stability frame. However, when simulating aircraft dynamics, it is useful to compute these forces in the body frame. In this way, the total force acting on the aircraft, consisting of aerodynamic, propulsive, and gravitational components, can be more easily calculated.

Starting from the stability frame coefficients (C_D, C_L), the body frame coefficients (C_X, C_Z) can be acquired by a change in direction and a rotation $\boldsymbol{R}_b^{s\top}$ through the angle of attack α. The rotation matrix is defined as follows:

$$\boldsymbol{R}_b^s(\alpha) = \begin{bmatrix} \cos(\alpha) & 0 & \sin(\alpha) \\ 0 & 1 & 0 \\ -\sin(\alpha) & 0 & \cos(\alpha) \end{bmatrix}, \tag{19}$$

and the transformation is then computed as

$$\begin{bmatrix} C_X \\ C_Y \\ C_Z \end{bmatrix} = \boldsymbol{R}_b^{s\top}(\alpha) \begin{bmatrix} -C_D \\ C_Y \\ -C_L \end{bmatrix}. \tag{20}$$

Given C_X and C_Z, the aerodynamic forces $\boldsymbol{F}_{\text{aero}}^b$ can be computed as

$$\boldsymbol{F}_{\text{aero}}^b = \bar{q}S \begin{bmatrix} C_X \\ C_Y \\ C_Z \end{bmatrix}, \tag{21}$$

where $\bar{q} = \frac{1}{2}\rho V_a^2$ is the dynamic pressure. Computation of the aerodynamic moments $\boldsymbol{M}_{\text{aero}}^b$ and the propulsion force $\boldsymbol{F}_{\text{prop}}^b$ can be done directly in the body frame, while the gravity force has to be transformed from NED to body

$$\boldsymbol{M}_{\text{aero}}^b = \bar{q}S \begin{bmatrix} bC_l \\ \bar{c}C_m \\ bC_n \end{bmatrix} \quad , \quad \boldsymbol{F}_{\text{prop}}^b = \begin{bmatrix} T \\ 0 \\ 0 \end{bmatrix} \quad , \quad \boldsymbol{F}_{\text{gravity}}^b = \boldsymbol{R}_b^{n\top} \begin{bmatrix} 0 \\ 0 \\ mg \end{bmatrix},$$

where $\boldsymbol{R}_b^n$ is the body to NED rotation matrix.

With all components decomposed in the body frame, the total forces $\boldsymbol{F}^b$ and moments $\boldsymbol{M}^b$ can be added together

$$\boldsymbol{F}^b = \boldsymbol{F}_{\text{aero}}^b + \boldsymbol{F}_{\text{prop}}^b + \boldsymbol{F}_{\text{gravity}}^b \tag{22a}$$

$$\boldsymbol{M}^b = \boldsymbol{M}_{\text{aero}}^b + \boldsymbol{M}_{\text{prop}}^b. \tag{22b}$$

2.3.4 Simulation

In dynamic simulations, we typically establish the starting point within an inertial world frame, such as the NED frame. To describe the motion of a rotating body within this inertial frame, we rely on Newton's second law of motion

$$\boldsymbol{F}^b = m(\dot{\boldsymbol{v}}_{nb}^b + \boldsymbol{\omega}_{nb}^b \times \boldsymbol{v}_{nb}^b) \tag{23a}$$

$$\boldsymbol{M}^b = \boldsymbol{I}\dot{\boldsymbol{\omega}}_{nb}^b + \boldsymbol{\omega}_{nb}^b \times \boldsymbol{I}\boldsymbol{\omega}_{nb}^b, \tag{23b}$$

where $\boldsymbol{I}$ is the inertia matrix. For aircraft, the moments of inertia are often assumed symmetric about the body $x - z$ plane [31], such that $I_{xy} = I_{yz} = 0$, resulting in

$$\boldsymbol{I} = \begin{bmatrix} I_x & 0 & -I_{xz} \\ 0 & I_y & 0 \\ -I_{xz} & 0 & I_z \end{bmatrix}. \tag{24}$$

With body frame forces and moments available from Eqs. (22a) and (22b), Newton's second law of motion can be reformulated to compute updates of the linear and angular accelerations

$$\dot{\boldsymbol{v}}_{nb}^b = \frac{1}{m}\boldsymbol{F}^b - \boldsymbol{\omega}_{nb}^b \times \boldsymbol{v}_{nb}^b \tag{25a}$$

$$\dot{\boldsymbol{\omega}}_{nb}^b = \boldsymbol{I}^{-1}(\boldsymbol{M}^b - \boldsymbol{\omega}_{nb}^b \times \boldsymbol{I}\boldsymbol{\omega}_{nb}^b), \tag{25b}$$

and based on $\boldsymbol{v}_{nb}^b$ and $\boldsymbol{\omega}_{nb}^b$, the position $\boldsymbol{p}_{nb}^n$ and attitude $[\phi, \theta, \psi]$ dynamics can be computed in the NED frame as shown in [30, Chap. 2]

$$\dot{\boldsymbol{p}}_{nb}^n = \boldsymbol{R}_b^n \boldsymbol{v}_{nb}^b \tag{26}$$

$$\begin{bmatrix} \dot{\phi} \\ \dot{\theta} \\ \dot{\psi} \end{bmatrix} = \begin{bmatrix} 1 & \sin\phi\tan\theta & \cos\phi\tan\theta \\ 0 & \cos\phi & -\sin\phi \\ 0 & \sin\phi/\cos\theta & \cos/\cos\theta \end{bmatrix} \boldsymbol{\omega}_{nb}^b. \tag{27}$$

The equivalent quaternion-based solution can also be found in [30, Chap. 2].

2.3.5 Electric propulsion system model

When the motor speed measurement Ω_p is not available, an electric propulsion system model can be used to calculate the speed. This model takes the power supply voltage U_b and throttle δ_t as input, and then outputs the motor acceleration $\dot{\Omega}_p$, which reflects the balance between the generated motor torque Q_m on one side and the load propeller torque Q on the other side. Mathematically, a simplified model of these relations can be formulated as follows:

$$U = \delta_t U_b \tag{28a}$$

$$I_m = (U - \Omega_p K_E)R^{-1} \tag{28b}$$

$$Q_m = I_m K_E, \tag{28c}$$

where U_b is the voltage of the battery or power supply, U and I_m are the voltage and current of the motor, R is the electric resistance of the motor, and K_E is the back-emf constant. An assumption necessary for this model is that the current varies slowly, allowing us to remove the motor inductance from the voltage-balance equation. The presented model can accurately replicate the steady-state response; however, some errors are expected in the transient behavior, particularly with voltage peaks during setpoint changes. Furthermore, a zero load current, I_{m0}, can be added to the torque model as $Q_m = (I_m - I_{m0})K_E$. However, in this case, it was assumed to be negligible to keep the model complexity low. Given the motor torque Q_m from (28 and the load torque Q from the aerodynamic propeller model (6, motor acceleration can be calculated

$$\dot{\Omega}_p = (Q_m - Q) I_p^{-1}, \tag{29}$$

which in simulation is used to compute the motor speed through numeric integration. An in-depth look at the electric propulsion system modeling can be found in [32, 33].

When analyzing a propulsion system, it is useful to compute both input and output power. For an electric motor, the input power is given by the electric power formula: $P_{el} = U \cdot I_m$. Conversely, the output power is the mechanical power generated, expressed as $P_m = Q \cdot \Omega_p$. In cases where direct measurements of motor voltage and current are unattainable, the power supplied by the battery $P_b = U_b \cdot I_b$ can serve as a viable approximation for input power, where the main uncertainty in the approximation arises from power losses in the electronic speed controller. Finally, provided the input and output power, the motor efficiency can be computed from the ratio P_m/P_{el}.

2.4 Extraction of the measured aerodynamic forces and moments

The process of aircraft system identification is greatly simplified when we have access to measurements or estimates of aerodynamic forces and moments. Although not required by the classical OEM, these data allow for a deeper understanding of the model's strengths and weaknesses by enabling individual comparison of the resulting force and moment coefficients. Furthermore, access to aerodynamic coefficients, as presented in Eqs. (33) and (34), makes it possible to use the hybrid OEM described in [35]. In hybrid OEM, indirectly measured aerodynamic coefficients are used as weighted outputs, which, in this work, has greatly improved parameter convergence during the system identification process. The remainder of this subsection presents the relations necessary to extract these aerodynamic

coefficients and perform system identification based on the measurements available in a standard flight log.

The main sensor that allows us to extract the force and moment coefficients from the flight data is the IMU, which typically includes a gyroscope and an accelerometer. The gyroscope measures angular rates $\boldsymbol{\omega}_{nb}^b = [p, q, r]^\top$, while the accelerometer measures the specific force $\boldsymbol{f}_{nb}^b = [a_x, a_y, a_z]^\top$, defined as a nongravitational force per unit mass [30, Chap. 14]. More specifically, it measures the inertial acceleration of the aircraft in the body frame, excluding gravitational acceleration. Mathematically, the accelerometer measurements are related to the total force as follows:

$$m\boldsymbol{f}_{nb}^b = \boldsymbol{F}^b - \boldsymbol{F}_{gravity}^b = \boldsymbol{F}_{aero}^b + \boldsymbol{F}_{prop}^b. \tag{30}$$

By rewriting (30, and using the definition from (21, the aerodynamic force coefficients can be obtained as a function of the measured accelerations

$$\begin{bmatrix} C_X \\ C_Y \\ C_Z \end{bmatrix} = \frac{1}{\bar{q}S}\left(m\boldsymbol{f}_{nb}^b - \boldsymbol{F}_{prop}^b \right). \tag{31}$$

Similarly, by combining Eqs. (23b) and (22b), the aerodynamic moment coefficients can be obtained as a function of the measured angular rates

$$\begin{bmatrix} C_l \\ C_m \\ C_n \end{bmatrix} = \frac{1}{\bar{q}S}\begin{bmatrix} \frac{1}{b} \\ \frac{1}{\bar{c}} \\ \frac{1}{b} \end{bmatrix}\left(\boldsymbol{I}\dot{\boldsymbol{\omega}}_{nb}^b + \boldsymbol{\omega}_{nb}^b \times \boldsymbol{I}\boldsymbol{\omega}_{nb}^b - \boldsymbol{M}_{prop,rear}^b \right). \tag{32}$$

Equations (31) and (32) can also be written out as a system of equations

$$C_X = \frac{(ma_x - T)}{\bar{q}S} \tag{33a}$$

$$C_Y = \frac{ma_y}{\bar{q}S} \tag{33b}$$

$$C_Z = \frac{ma_z}{\bar{q}S} \tag{33c}$$

$$C_l = \frac{1}{\bar{q}Sb}\left[I_x\dot{p} - I_{xz}(pq + \dot{r}) + (I_z - I_y)qr + Q + I_p\dot{\Omega}_p \right] \tag{33d}$$

$$C_m = \frac{1}{\bar{q}S\bar{c}}\left[I_y\dot{q} + (I_x - I_z)pr + I_{xz}(p^2 - r^2) + I_p\Omega_p r \right] \tag{33e}$$

$$C_n = \frac{1}{\bar{q}Sb}\left[I_z\dot{r} - I_{xz}(\dot{p} - qr) + (I_y - I_x)pq - I_p\Omega_p q \right]. \tag{33f}$$

The transformation from body frame to stability frame is as follows (20):

$$\begin{bmatrix} C_D \\ C_Y \\ C_L \end{bmatrix} = \boldsymbol{R}_b^s(\alpha) \begin{bmatrix} -C_X \\ C_Y \\ -C_Z \end{bmatrix}. \tag{34}$$

3 Experiment setup and data analysis

This section describes the flight and wind tunnel experiments used to model and identify the Skywalker X8 UAV model. Specifically, the system identification maneuvers and the measured data are described. In addition, sources of measurement uncertainty are presented.

3.1 Maneuver design

The choice of maneuver periods and amplitudes was based on frequency response analysis conducted on prior models of the Skywalker X8 UAV [8, 9]. The analysis was performed as part of a master's thesis work by Trondstad [36] who concluded that the main frequency response of the Skywalker X8 should be in the region of 1 to 10 rad/s.

Table 3 Overview of the performed system identification maneuvers

Direction	Type	Pulse duration (s)	Amplitude °	Air-speed (m/s)	Number of experiments
Lateral	*1-2-1*	0.3	15	18	7
Lateral	Doublet	0.4	15	18	5
Longitudinal	*3-2-1-1*	0.3	10	18	8
Longitudinal	Doublet	0.4	15	18	8

The findings were obtained based on coefficients from [9] using the Marchand method as described in [11, Chap 2.III]. This information was then used to select the pulse durations for the system identification maneuvers presented in Table 3. The duration of the pulse corresponds to the length of a single deflection in a maneuver. The relation of pulse durations to the excited frequencies of vehicle dynamics is described in [11, Chap. 2.III]. For example, for a doublet with pulse width of 0.4 s, the mean excited frequency is about 2.3/0.4 = 5.75 rad/s. For more complex maneuvers, such as *3-2-1-1* and *1-2-1*, the frequency response has several peaks, and the range of frequencies is more meaningful to specify in that case.

A hard constraint on the length of the maneuver period is related to the line-of-sight operation of the UAV. The longest straight part of the trajectory flown by the UAV during testing was about 400 m, allowing for one or two 10-s maneuvers. As a result, combining the time for maneuvering, settling, and maintaining steady flight before and after a maneuver can easily exceed 30 s for the slow mode maneuvers, pushing against the 400 m constraint. This makes exciting the slow dynamic modes, such as the phugoid and spiral diverse modes, more challenging, as the corresponding mode periods can be larger than 10 s. Due to this limitation, the identified coefficients associated with the slow dynamic modes are expected to have higher uncertainty relative to the other aerodynamic coefficients. Additionally, the absence of a rudder on the Skywalker X8 makes it challenging to excite pure yaw dynamics, further contributing to the uncertainty in the aerodynamic coefficients, particularly those related to spiral divergence mode.

3.2 Flight experiments

The test campaign took place at the Breivika airfield in Agdenes, Norway, in May 2023. The maneuvers were carried out during two 30-min flights, where the UAV flew in

Fig. 2 Visualization of the UAV flight path during flight experiments

(a) Flight path of the UAV in red. The image was extracted from the Mission Planner software. The time-averaged wind direction is visualized in turquoise.
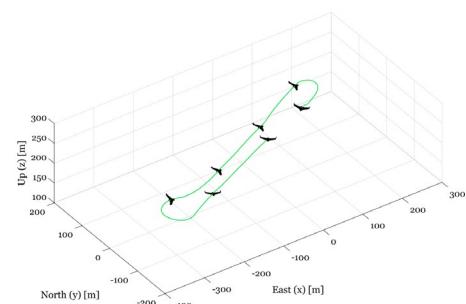
(b) Animated 3D flight path created using [37].

Table 4 Sensor overview

Sensor	Selected accuracy metrics
Cube orange	
ICM-20602 IMU	Gyroscope noise: ± 4mdps/$\sqrt{Hz}$, Accelerometer noise: $100\mu g/\sqrt{Hz}$
ICM20948 IMU/ Magnetometer	Gyroscope noise: ± 15mdps/$\sqrt{Hz}$, Accelerometer noise: $230\mu g/\sqrt{Hz}$
	Magnetometer resolution: 16-bit, Magnetometer range: ± 4900 μT
MS5611 barometer	Accuracy at 25°C, 750 mbar: ± 1.5 mbar
Here3+ GNSS	Positioning accuracy: 0.025 m
Airspeed sensor MS4525DO	Pressure accuracy: $\pm 0.25\%$ from the best fit over the pressure range at 25°C
STIM300	
Accelerometer	Bias instability—0.02 mg, velocity random walk—0.03 m/s/$\sqrt{h}$
Gyroscope	Bias instability—0.3 °/h, angular random walk—0.15 °/$\sqrt{h}$

a predetermined flight path, as shown in Fig. 2a. The estimated position and attitude data have been validated by recreating the flight path in a 3D animation shown in Fig. 2b.

3.3 Payload and sensors

The payload and sensors installed on the Skywalker X8 are based on the setup in [38]. The Skywalker X8 flight stack is built around the Cube Orange autopilot, which runs on the open-source ArduPilot firmware. The Cube Orange comprises triple redundant IMUs with magnetometers and pressure sensors. In addition, the Skywalker X8 has a pitot-static tube for airspeed measurement, and a global navigation satellite system (GNSS) receiver for positioning. Furthermore, the ArduPilot firmware provides state estimates computed using an EKF, which includes estimates of the wind velocity vector, the angle of attack, and the sideslip angle. Moreover, an external IMU, STIM300, was installed for redundancy.

Table 4 presents a summary of the sensors installed on the Skywalker X8 UAV used in the experiments, along with the relevant accuracy metrics sourced from their respective data sheets.

3.4 Data pre-processing

Resampling and filtering of the data were performed prior to the calculations and transformations described in Sect. 2. More specifically, all measurements and estimates were resampled to a common frequency of 40 Hz set by the ArduPilot EKF. Furthermore, angular accelerations, used to calculate aerodynamic moments in (33), were obtained through smoothed numerical differentiation of angular velocities, as recommended in [10, Chap. 5.1.7].

During the flight, the EKF estimated a strong north-west wind of 9 m/s. The experimental data did not include measurements of the angle of attack, and the EKF only estimated horizontal wind, making it challenging to directly identify the trim angle of attack. This challenge was addressed using data from previous Skywalker X8 flights conducted by Borup et al. [39] with a five-hole probe. By referencing these flights, we extracted additional information from our data. Specifically, assuming a steady vertical wind, we used the relative velocity estimates in the horizontal plane and the measured airspeed to obtain a correction term equivalent to a vertical wind component of 2.8 m/s. To assess the credibility of the computed wind correction, we compared the resulting air data, shown in Fig. 3, with the reference flight data in [39, Fig. 11]. Based on this comparison, the combination of an angle of attack of 8° at an airspeed of 18 m/s was deemed credible, validating the computed wind correction.

In general, using advanced measurement equipment, such as a five-hole probe, on small low-cost UAVs is quite challenging. Due to the small size, it might be difficult to find an appropriate mounting location for the probe and correct for potential measurement uncertainties caused by mounting errors. Furthermore, for small UAVs, the sensor might be several times more expensive than the platform itself, substantially increasing the economic risk associated with the
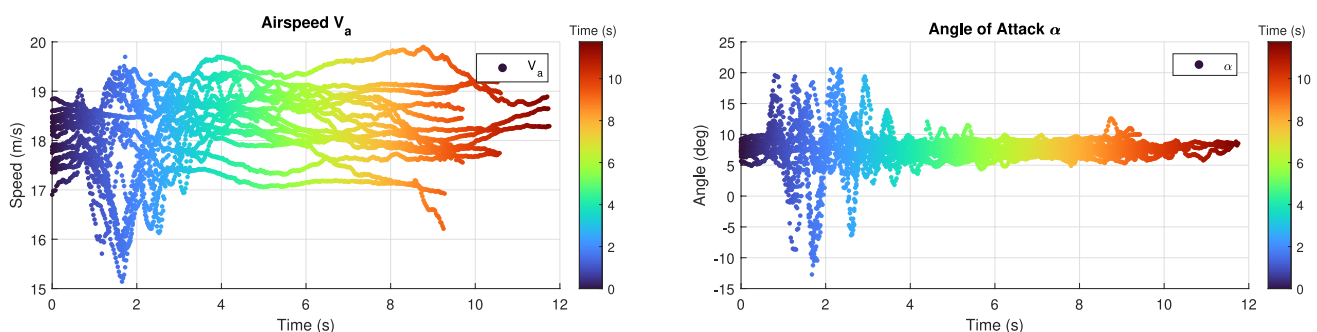
Fig. 3 Measured airspeed V_a and estimated angle of attack α of the Skywalker X8 UAV. The air data are comparable to the flight test results seen in [39] where a five-hole air probe was used to measure α directly

experiments. Based on previous system identification experience on the same platform [9], and due to the mentioned concerns, we decided to use the air data estimates provided by the ArduPilot EKF instead of flying with the five-hole air probe. Furthermore, results from previous flights with the five-hole probe [39] provide a good reference point to validate the current air data estimates. The drawback of using an EKF-estimated angle of attack and sideslip angle is that these estimates have varying certainty depending on the wind conditions and the complexity of the performed maneuver. This is important to consider when discussing the model prediction results in regions far from the trim point.

3.5 Data selection

Initial screening of the experiment data is performed using the drag and lift curves in Fig. 4. First- and second-order polynomials were fitted to the data to highlight the measured mean and variance. The lift and drag curves exhibit plausible trends, yet two points should be discussed in greater detail.

(1) According to the wind tunnel tests and analysis in [8, 9], the Skywalker X8 should have a positive lift at $\alpha = 0$ with $C_{L0} = 0.058$. However, the flight data in this article indicate a negative lift coefficient at $\alpha = 0$. Although this could be true for the particular Skywalker X8 used in this study, due to dents and other damage related to previous crashes, it could also be a result of uncertainties in the vertical wind estimates, which directly affect the computed α, Eqs. (15) and (16). On the other hand, as presented earlier, the directly measured air data in [39] are similar to the airspeed and angle of attack presented here. Moreover, according to the authors of [8], there were uncertainties related to the selection of the zero angle of attack setting in the wind tunnel. Another relevant input is the elevator deflection; due to a strong vertical wind of -2.8 m/s during the experiments, the

UAV was flying with a nonzero elevator deflection, which shifts the whole lift curve down, thus explaining some of the discrepancies between the flight data and the wind tunnel tests.

(2) There are several data points in Fig. 4a that indicate negative drag values. Negative drag is not physical and can be explained by a combination of uncertainties in the accelerometer measurement, the thrust force compensation done in (33b), and angle of attack estimates. The unmodeled part of the coupling between the drag and the thrust force could also explain some uncertainty. This is, however, expected when analyzing flight data of a small fixed-wing aircraft such as the Skywalker X8. An aircraft with a relatively large wing area and a small weight of 3.4 kg is highly susceptible to gusts and wind disturbances, which increases the likelihood of encountering aerodynamic states far out of trim.

To analyze the quality of the initial Skywalker X8 model, an analysis of the model prediction residuals was performed. The results of the analysis are presented later in Sect. 4.1.1, revealing a greater uncertainty in the model predictions for the drag and side force. As such, the drag and side force coefficients were considered more thoroughly in the second round of data pre-processing. In practice, this means that maneuvers with inconsistent drag values as well as maneuvers initiated at high sideslip angles or significant angular rates were dismissed. In total, of the 28 recorded maneuvers, 17 were selected for system identification, with a further split into 13 maneuvers for training and 4 for validation. By definition, the validation set maneuvers were not used in the model identification process.

The training and validation split, with the identified coefficients and the associated weighted output, is presented in Table 5. Notice that the aerodynamic coefficients are part of the weighted outputs, consistent with the hybrid OEM,

(a) C_L vs C_D (b) C_L vs α (c) C_m vs α
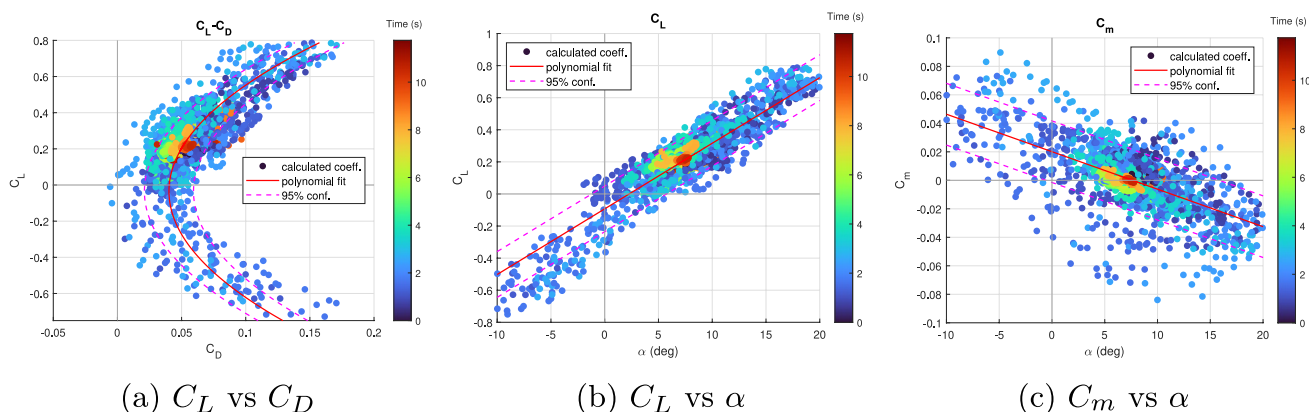
Fig. 4 Drag, lift, and pitch moment curves computed from the the training and validations sets presented in Table 5. The coefficients are computed as shown in Eqs. (33) and (34). The color indicates which part of the maneuver the data point is taken from with Fig. 3 as the reference. Focusing on the scatter points in red provides a good indication of the Skwylaker X8's trim condition flying at 18 m/s

Table 5 Aerodynamic parameters and the weighted outputs used to estimate these parameters

Training data	Validation data	Parameters	Weighted outputs	Parameters	Weighted outputs
$3 \times$ long. *3-2-1-1* $3 \times$ long. doublet	$1 \times$ long. *3-2-1-1* $1 \times$ long. doublet		z, θ		z, ϕ, ψ
		$C_{D(*)}$	u, w, q	$C_{Y(*)}$	v, p, r
		$C_{L(*)}$	a_x, a_z	$C_{l(*)}$	a_y
$4 \times$ lat. *1-2-1* $3 \times$ lat. doublet	$1 \times$ lat. *1-2-1* $1 \times$ lat. doublet	$C_{m(*)}$	V_a, α	$C_{n(*)}$	V_a, β
			$C_{\{D,L,m\}}$		$C_{\{Y,l,n\}}$

The weighted outputs are grouped for readability. The force and moment coefficients are computed from the state variables, as shown in Eqs. (33) and (34)

Table 6 Propeller thrust and torque coefficients used in Eqs. (8) and (9)

C_T		C_Q	
C_{T0}	0.1400	C_{Q0}	0.0082
C_{T1}	−0.0300	C_{Q1}	0.0112
C_{T2}	−0.2370	C_{Q2}	−0.0211
C_{T3}	0.0847		

Table 7 Propulsion system parameters

Name and symbol		Value
Back-EMF constant	k_E	0.0157 V/(rad/s)
Motor resistance	R	0.017 Ω
Propeller diameter	D	14″ or 0.3556 m
Propeller inertia	I_p	3.46×10^{-4} kg m²

discussed in Sect. 2.4. Estimation was performed separately for the longitudinal and lateral coefficients, while the 13 selected maneuvers were kept the same.

3.6 Propulsion system model

The propulsion system of the Skywalker X8 UAV consists of an electric Hacker A40-12 S V2 14-pin KV610 motor, a Jeti SPIN Pro 66 speed controller, and a 14x8 Aeronaut CAM folding propeller. The propeller parameters presented in Tables 6 and 7 were identified separately based on wind tunnel experiments. The back-emf coefficient K_E and electrical resistance R of the motor are based on the specifications provided in the motor's datasheet.

Figure 5 displays measurements alongside model prediction results derived from multistep experiments conducted in a wind tunnel at a constant speed of 18 m/s. The identified model is a propulsion system model that takes power supply voltage and throttle as input and outputs the resulting motor acceleration. The motor acceleration is then integrated to get the motor speed, making it possible to compute propeller thrust and torque, as described in Sect. 2.3.5.

The motor speed was not measured during the Skywalker X8 flights; instead, the motor model in Sect. 2.3.5 was used to generate the propulsion system data. As part of the pre-processing step, a throttle offset was added to match the measured and simulated power consumption shown in

(a) Motor speed model.   (b) Propeller torque model.   (c) Propeller thrust model.
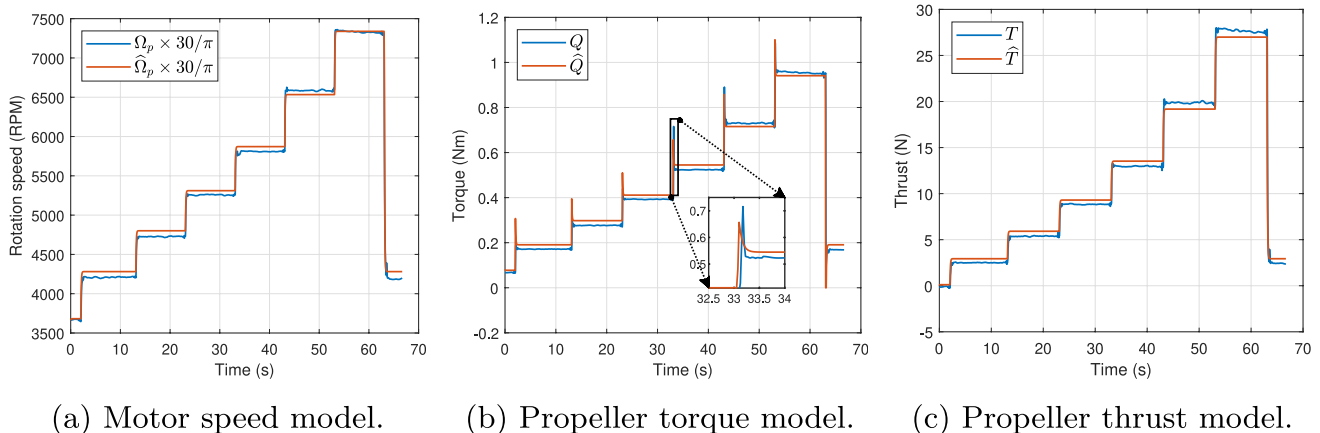
Fig. 5 Propeller model identified based on multistep experiments performed in a wind tunnel at a constant speed of 18 m/s. The spikes in the torque data (**b**) are due to the gyroscopic effect generated during acceleration as described in (11). Model prediction results are indicated by the ^ . The zoom plot in (**b**) is made using [40]

(a) Electrical power.

(b) Motor speed.

(c) Propeller throttle.

(d) Airspeed.

(e) Propeller torque.

(f) Propeller thrust.
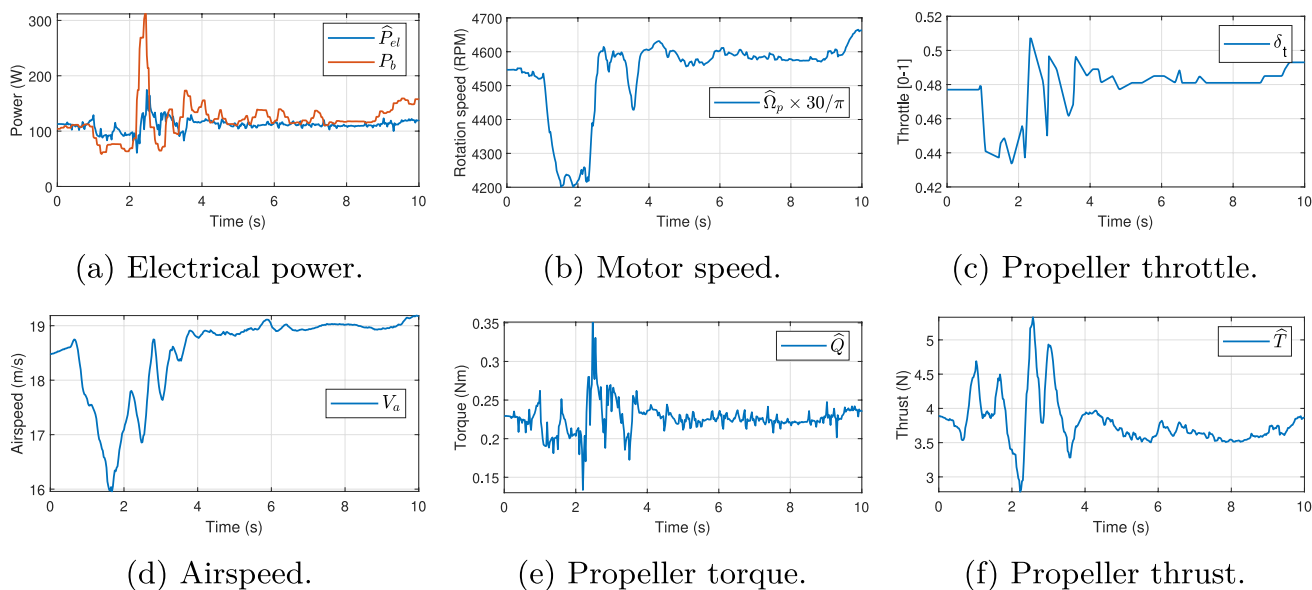
Fig. 6 Output of the propulsion system model for the Skywalker X8 used in system identification. Throttle, battery power, and airspeed are available from flight experiments, while the remaining data are generated by the model in Tables 6 and 7. The discrepancy in electrical power in **a** is due to a missing inductance in the model, as described in Sect. 3.6. The oscillations in thrust (**f**) and torque (**e**) carry over from both throttle (**c**) and airspeed (**d**); moreover, the sharp jumps in the torque are due to the gyroscopic effect described in (11

Fig. 6a. The resulting mapping from electric power P_{el} to motor speed was validated based on data from [33]. The model output for one of the experiments is shown in Fig. 6. Note that the power spike in Fig. 6a is not captured by the model. As described in Sect. 2.3.5, this is because the model assumes a slowly varying current and does not account for the effects of inductance during a setpoint change. Inductance opposes changes in current, resulting in a voltage spike necessary to overcome the inductive reactance. Consequently, this leads to a transient power spike seen in the measured data.

In the initial modeling, the variation of the battery voltage was assumed to be negligible. Upon further analysis of the prediction results, it was discovered that the drag model in particular had potential for improvement. The propulsion system is directly coupled to the drag model, prompting further consideration. As shown in Fig. 7, the battery voltage fluctuates between 15.2 V and 16.4 V which directly affects the mapping from the throttle to the power delivered to the motor, thus influencing the drag model. Consequently, the battery voltage was used as input in the system identification process for the updated model.

4 Results

This section presents the results of the aerodynamic modeling for the Skywalker X8 UAV. It is organized as follows: First, an analysis of the model prediction residuals is provided. This residual analysis has been crucial in identifying
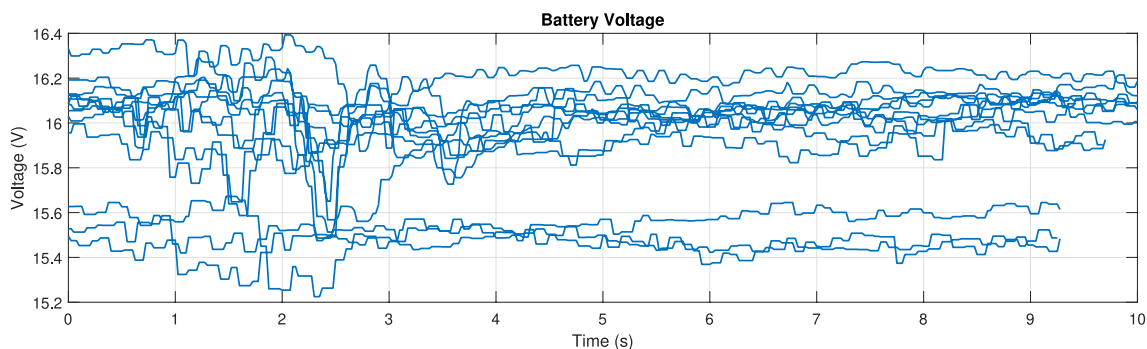
Fig. 7 Measured battery voltage variation during the maneuvers

weaknesses and refining the initial model. Next, the model prediction results are presented alongside the measured experiment data, and the new set of identified aerodynamic coefficients, used to generate the predictions, is provided. Finally, this section includes the results of linearization, comparing the predictions of the nonlinear and linearized models.

4.1 Model fitting results

The system identification process began with the initial parameters available from wind tunnel experiments presented in [8]; an intermediate model was then identified and used as a basis for model analysis. The analysis led to remodeling and improvement of the drag and side force models through a thorough outlier analysis, as well as a revision of the propulsion system model.

4.1.1 Model characteristics and residual analysis

The identified model structure follows Eqs. (17) and (18). A comparison between the aerodynamic coefficients calculated from the flight data and the coefficients obtained from the simulation of the model is presented in Fig. 8. In particular, the drag, lift, and pitch moment curves are shown. Although the presented scatter plots do not indicate the model's accuracy, they can provide a general understanding of the model's region of validity and the distribution of the measured data points. Visual analysis indicates a good model fit about the trim, indicated by the dense regions of the scatter plots. However, the model is not as good in the regions further away from the trim, which is especially visible at the negative angles of attack, where only limited amounts of data have been collected.

For a more quantitative analysis of the model, the residual distribution for each of the aerodynamic coefficients is shown in Fig. 9.

For most of the coefficients, the residuals are narrowly distributed about zero, indicating a good match between the data and the model. A quick look at the comparison between the initial and final models reveals that there are mainly two coefficient models that were improved—the drag and the side force. The double peak in the drag residual distribution indicates that the intermediate drag model has varying accuracy depending on the maneuver it predicts. The final model has a single peak and, as discussed in Sects. 3.5 and 3.6, the improvement of the model was achieved through better data pre-processing and a revised propulsion system model. Moreover, as discussed in the modeling section (Sect. 2.3.2), the drag and the side force are physically coupled through the sideslip angle, and although they are decoupled in the structure of the identified model, the residual distribution analysis shows how the improvement in the drag model also has a slight effect on the side force model.

4.1.2 Nonlinear model prediction analysis

The model prediction results for a longitudinal *3-2-1-1* and a lateral doublet maneuver are presented in Figs. 10 and 11. The evaluation of the model predictions can be split into two stages: the first, prediction of the aerodynamic forces and moments, and the second, prediction of the aircraft motion. Forces and moments are easier to model and identify, as direct measurements of aircraft acceleration and angular rates are available from the IMU. In contrast, the aircraft motion is based on the output of an EKF, which combines the airspeed, IMU, and GNSS measurements to estimate the wind and the resulting aerodynamic state of the aircraft, making the model prediction analysis more challenging due to uncertainties introduced by estimation.

(a) C_L vs C_D (b) C_L vs α (c) C_m vs α
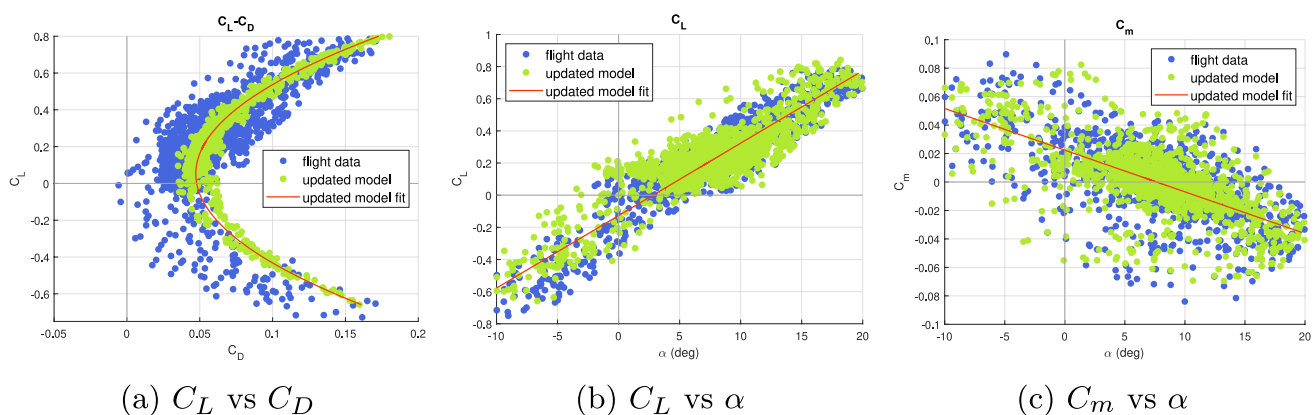
Fig. 8 Comparison of drag, lift, and pitch moment curves based on flight and simulation data of 17 maneuvers at 18 m/s. The red line shows the model output mean computed by fitting a polynomial to the output data

(a) $C_L - \widehat{C}_L$

(b) $C_D - \widehat{C}_D$

(c) $C_m - \widehat{C}_m$

(d) $C_Y - \widehat{C}_Y$

(e) $C_l - \widehat{C}_l$

(f) $C_n - \widehat{C}_n$
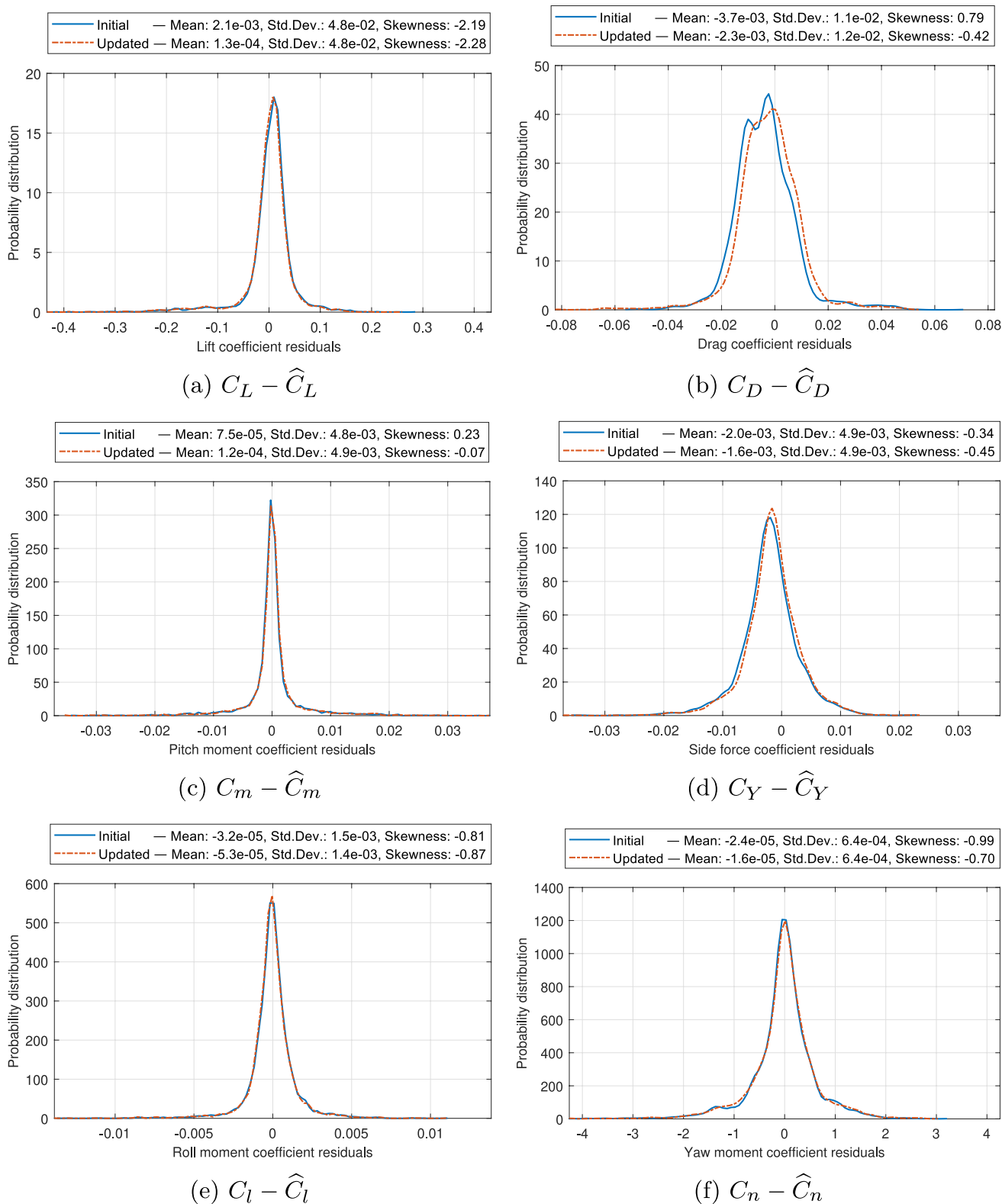
Fig. 9 Probability distribution of the aerodynamic coefficient residuals in the training set. The drag residuals show a biased distribution which warranted a further investigation of the initial identified model. The updated model provides an overall better result, particularly for drag and side force models
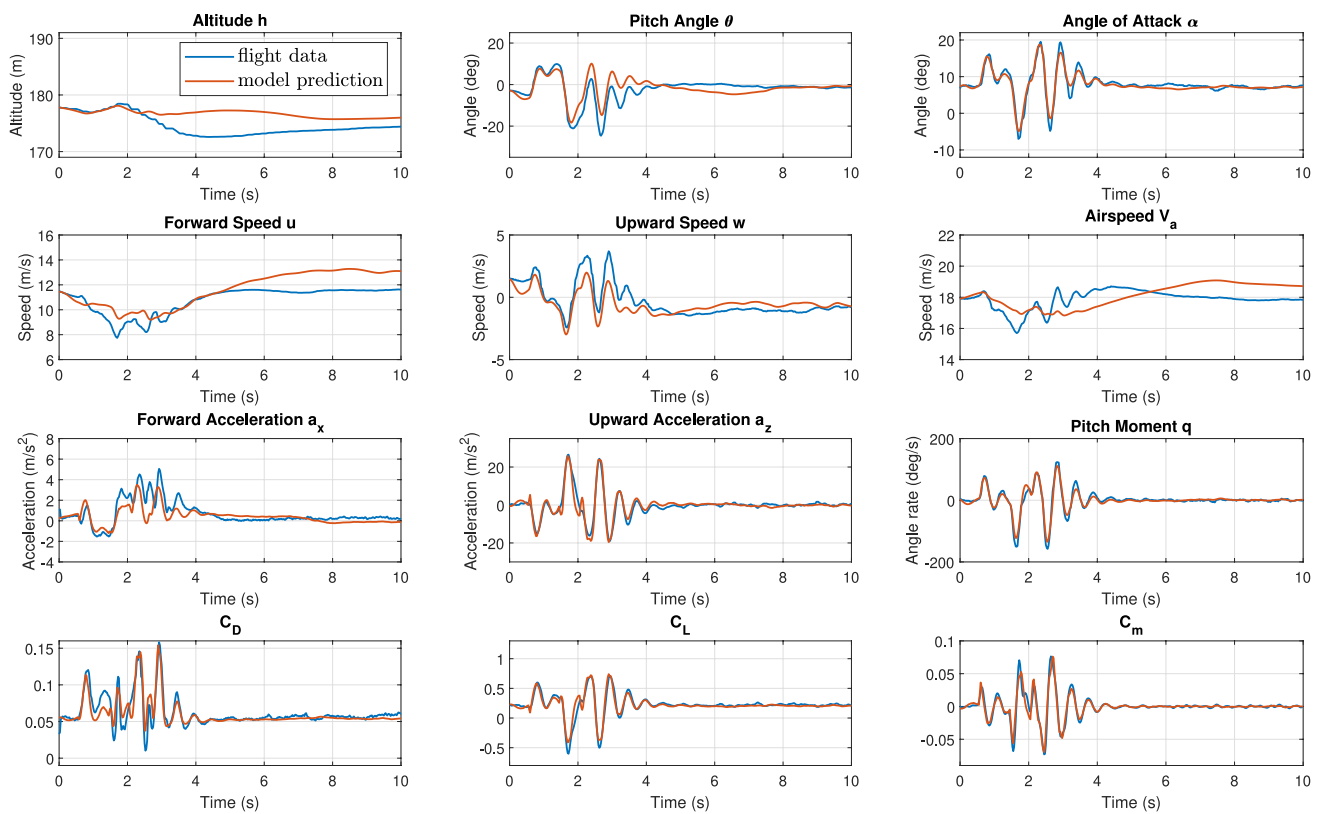
Fig. 10 Weighted outputs and the model prediction results for a longitudinal *3-2-1-1*-maneuver used in the identification of longitudinal parameters $C_{D(*)}$, $C_{L(*)}$, $C_{m(*)}$

(1) A look at the model prediction results for both lateral and longitudinal examples reveals that the model can predict the force and moment coefficients for the duration of the recorded maneuvers. In general, the model is able to replicate large dynamic movements with high accuracy; however, the prediction of the low amplitude dynamics is not as accurate. This is an expected result, as the measurement noise and environmental disturbances are difficult to replicate in simulation. When analyzing the individual force and moment coefficients, it is noticeable that the predicted drag peaks, both positive and negative, do not fully match the measurements in Fig. 10; however, as already discussed, modeling the drag can be challenging due to the coupling effects between the propulsion model and the airframe drag. Identification of an aero-propulsive model as suggested in [24] or a more in-depth modeling of the thrust compensation in (33b) can potentially be used to improve this modeling error. Additionally, using direct motor speed measurements rather than estimated values could further improve modeling accuracy.

(2) The second-stage results provide reasonably good predictions, especially for the angle of attack shown in Fig. 10. This is expected as α is directly related to the longitudinal force and moment coefficients. When it comes to altitude,

heading angle, and body frame speeds, the model predictions are less accurate. It should be noted that the wind makes the estimation and prediction much more challenging. Calm wind conditions should, therefore, be prioritized when performing system identification with small aircraft. Alternatively, direct measurements of α and β should be considered.

4.1.3 Identified model parameters

The final set of model parameters is presented in Table 8.

The coefficient and standard deviation values (StdDev.) were obtained using the Fitlab tool [19]. The model structure was identified through stepwise regression [10, Chap. 5], where regressors are gradually added to the model and several statistics, such as model prediction error, are analyzed to keep or discard a particular regressor. The low standard deviations in Table 8 indicate a good alignment between the data and the selected model structure. Although most coefficients are identified with a low standard deviation, there are some with higher uncertainty which are worth mentioning. In particular, this concerns coefficients related to the yaw dynamics, C_{Yr}, C_{lr}, C_{np}. As discussed previously in Sect. 3.1, this uncertainty can be explained by the lack of rudder on the Skywalker X8 UAV which makes it difficult to excite yaw dynamics in
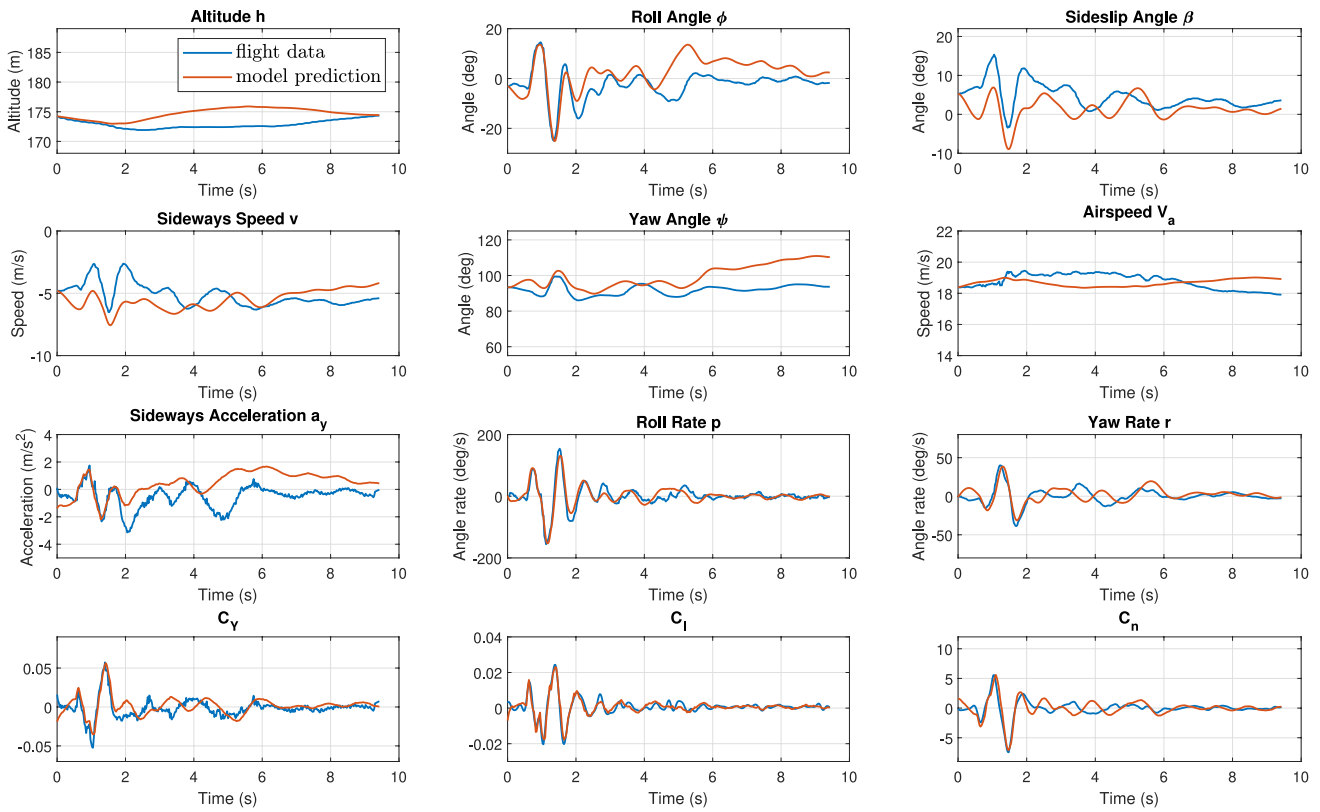
Fig. 11 Weighted outputs and the model prediction results for a lateral doublet maneuver used in the identification of lateral parameters $C_{Y(*)}, C_{l(*)}, C_{n(*)}$

Table 8 Identified coefficients of the nonlinear aerodynamic model given by Eqs. (17) and (18)

C_D				C_l			
Coeff.	Value	Std dev.	(Rel. %)	Coeff.	Value	Std dev.	(Rel. %)
C_{D0}	0.058	6.73e−04	(1.12)	C_{l0}	0.007	7.21e−05	(1.07)
C_{Dq}	0.480	5.85e−02	(10.54)	$C_{l\beta}$	−0.108	1.04e−03	(0.97)
C_{DCT}	−0.217	1.99e−02	(3.16)	C_{lp}	−0.313	2.91e−03	(0.93)
C_{Dk1}	−0.034	2.18e−03	(5.06)	C_{lr}	0.037	3.60e−03	(6.12)
C_{Dk2}	0.225	2.33e−03	(1.02)	$C_{l\delta a}$	0.102	8.51e−04	(0.83)
C_L				C_m			
C_{L0}	−0.077	3.04e−03	(3.68)	C_{m0}	0.027	2.81e−04	(1.10)
$C_{L\alpha}$	2.573	2.33e−02	(0.86)	$C_{m\alpha}$	−0.274	1.97e−03	(0.74)
C_{Lq}	17.119	2.30e−01	(1.24)	C_{mq}	−1.608	2.44e−02	(1.49)
$C_{L\delta e}$	1.369	2.03e−02	(1.23)	$C_{m\delta e}$	−0.276	1.89e−03	(0.68)
C_Y				C_n			
C_{Y0}	0.011	1.91e−04	(1.72)	C_{n0}	−6.3e−04	9.51e−06	(1.57)
$C_{Y\beta}$	−0.285	3.08e−03	(1.09)	$C_{n\beta}$	0.022	1.61e−04	(0.76)
C_{Yp}	−0.270	7.67e−03	(2.93)	C_{np}	−0.009	5.27e−04	(5.27)
C_{Yr}	0.108	1.20e−02	(8.51)	C_{nr}	−0.050	5.34e−04	(1.13)
$C_{Y\delta a}$	0.097	2.24e−03	(2.34)	$C_{n\delta a}$	−0.007	1.48e−04	(2.45)

The coefficients were identified according to Table 5, based on flight maneuvers performed at the speed of 18 m/s. The (Rel. %) column shows the standard deviation as a percentage of the coefficient value

isolation and identify the associated coefficients. Nonetheless, as shown in Fig. 11, the identified lateral model is able to match the large-amplitude dynamics quite well.

Analysis of Table 8, or equivalently Eqs. (17) and (18), shows that the identified model is for the most part linear, except for the drag, which is modeled as a second-order function of lift and includes a propeller thrust component. The negative thrust component indicates that the drag decreases with increased throttle, i.e., the propeller has an impact on the flow across the airframe.

4.1.4 Actuators

In addition to the aerodynamic model, two actuator models had to be implemented to obtain a complete simulation-ready model of the Skywalker X8 UAV. Following [8], a second-order process was used to model the elevon dynamics and a first-order process was used to model the throttle input. Both models include input delays, identified by matching control inputs to the measured IMU-data, i.e., the time from a change in a control signal to a change in the measured acceleration or angular rate. The complete set of actuator model parameters is listed in Table 9.

4.2 Linearized dynamics

It is often useful to describe a dynamic system with a linear model. Linear models have numerous applications: they enable faster simulations, facilitate the application of well-established linear control design methods, and unlock tools for frequency-domain analysis such as transfer function evaluation, and the assessment of system poles and zeros. The frequency-domain analysis is particularly useful in aircraft analysis, as decades of research have resulted in a large amount of knowledge relating aerodynamic modes, i.e., the location of system poles and zeros to the aircraft flight characteristics. Chapters 10 and 11 of [41] provide a good introduction to this type of analysis.

A linearized model can be represented using the state-space formulation as follows:

$$\dot{x} = Ax + Bu \quad , \quad y = Cx, \tag{35}$$

where A, B, C are the system matrices, x is the system state, u is the input, and y is the output.

The system matrices for the lateral and longitudinal dynamics were computed by linearizing the equations of motion in

(25. The linearization process was also performed using the `linmod` function in the Matlab Simulink library to validate the results derived manually.

A realization of the linearized system dynamics is presented in state-space form in Eqs. (39) to (42). The results show a linearization about the trim point taken from the *3-2-1-1*-maneuver in Fig. 10. The poles of the system are shown in Fig. 12. The trim state and input are

$$x^* = \begin{bmatrix} u^* & v^* & w^* & p^* & q^* & r^* & h^* & \phi^* & \theta^* & \psi^* \end{bmatrix}^\top$$
$$= \begin{bmatrix} 11.8\,\text{m/s} & -6.26\,\text{m/s} & -0.28\,\text{m/s} & 0 & 0 & 0 & 178\,\text{m} & -0.47° & -1.11° & 92.89° \end{bmatrix}^\top \tag{36}$$

$$u^* = \begin{bmatrix} \delta_e^* & \delta_a^* & \delta_t^* & u_w^* & v_w^* & w_w^* \end{bmatrix}^\top$$
$$= \begin{bmatrix} -2.35° & -2.16° & 0.44 & -5.93\,\text{m/s} & -6.62\,\text{m/s} & -2.75\,\text{m/s} \end{bmatrix}^\top. \tag{37}$$

The described trim state and input represent the following flight condition:

$$\begin{bmatrix} V_a & \alpha & \beta & \gamma \end{bmatrix}^\top = \begin{bmatrix} 17.9\,m/s & 7.9° & 1.2° & 0.0° \end{bmatrix}^\top. \tag{38}$$

4.2.1 Lateral dynamics

$$x_{lat} = \begin{bmatrix} v & p & r & \phi & \psi \end{bmatrix}^\top \quad , \quad u_{lat} = \begin{bmatrix} \delta_a & u_w & v_w & w_w \end{bmatrix}^\top \tag{39}$$

$$A_{lat} = \begin{bmatrix} -0.68 & -0.96 & -11.52 & 9.82 & 0 \\ -5.45 & -16.81 & 1.80 & 0 & 0 \\ 0.53 & -1.62 & -2.10 & 0 & 0 \\ 0 & 1 & 0 & 0 & 0 \\ 0 & 0 & 1 & 0 & 0 \end{bmatrix},$$

$$B_{lat} = \begin{bmatrix} 4.17 & -0.02 & 0.68 & -0.003 \\ 92.93 & -0.24 & 5.45 & -0.03 \\ 1.64 & -0.003 & -0.53 & 0 \\ 0 & 0 & 0 & 0 \\ 0 & 0 & 0 & 0 \end{bmatrix} \tag{40}$$

$$C_{lat} = I_{5\times5}.$$

Table 9 Actuator model parameters for a second-order servo system controlling the elevons and a first-order system for the throttle control

Servo 2nd order system			Throttle 1st order system	
Natural frequency	Damping	Input delay	Time constant	Input delay
100 rad/s	0.707	0.07 s	0.2 s	0.05 s

Table 10 Lateral poles at 18 m/s

Pole	Damping	Frequency (rad/s)	Period (s)
$-17.50 + 0.00i$	1	17.50	0.36
$-0.84 + 3.73i$	0.22	3.83	1.64
$-0.84 - 3.73i$	0.22	3.83	1.64
$-0.42 + 0.00i$	1	0.42	14.96

Table 11 Longitudinal poles at 18 m/s

Pole	Damping	Frequency (rad/s)	Period (s)
$-6.19 + 4.93i$	0.78	7.92	0.79
$-6.19 - 4.93i$	0.78	7.92	0.79
$-0.22 + 0.97i$	0.22	0.99	6.35
$-0.22 - 0.97i$	0.22	0.99	6.35

4.2.2 Longitudinal dynamics

$$\boldsymbol{x}_{lon} = \begin{bmatrix} u & w & q & \theta \end{bmatrix}^\top \quad , \quad \boldsymbol{u}_{lon} = \begin{bmatrix} \delta_e & \delta_t & u_w & v_w & w_w \end{bmatrix}^\top \quad (41)$$

$$A_{lon} = \begin{bmatrix} -0.59 & 0.92 & 0.61 & -9.82 \\ -0.23 & -6.31 & 4.42 & 0.19 \\ 0.78 & -5.59 & -5.92 & 0 \\ 0 & 0 & 1 & 0 \end{bmatrix}, \ B_{lon} = \begin{bmatrix} 4.26 & 19.43 & 0.59 & 0.01 & -0.92 \\ -58.88 & 0.25 & 0.23 & 0.02 & 6.31 \\ -101.91 & 0 & -0.78 & 0 & 5.59 \\ 0 & 0 & 0 & 0 & 0 \end{bmatrix}$$

$$(42)$$

$$C_{lon} = I_{4\times4}.$$

4.2.3 Coupled dynamics

For the coupled dynamics, the model includes the effect of lateral states on the longitudinal states and vice versa. For instance, in the linear system realization given by (43, the forward acceleration $\dot{u}$ is a function of the yaw rate r and, similarly, the sideways acceleration $\dot{v}$ is a function of the forward velocity u

$$\boldsymbol{x} = \begin{bmatrix} u & v & w & p & q & r & \phi & \theta & \psi \end{bmatrix}^\top \quad , \quad \boldsymbol{u} = \begin{bmatrix} \delta_e & \delta_a & \delta_t & u_w & v_w & w_w \end{bmatrix}^\top$$

$$(43)$$

$$A = \begin{bmatrix} -0.59 & -0.01 & 0.92 & 0 & 0.61 & -6.26 & 0 & -9.82 & 0 \\ 0.02 & -0.68 & 0 & -0.96 & 0 & -11.52 & 9.82 & -0.00 & 0 \\ -0.23 & -0.02 & -6.31 & 6.26 & 4.42 & 0 & 0.08 & 0.19 & 0 \\ 0.24 & -5.45 & 0.03 & -16.81 & 0 & 1.80 & 0 & 0 & 0 \\ 0.78 & 0 & -5.59 & 0 & -5.92 & 0 & 0 & 0 & 0 \\ 0 & 0.53 & 0 & -1.62 & 0 & -2.10 & 0 & 0 & 0 \\ \mathbf{0}_{3\times3} & & & \boldsymbol{I}_{3\times3} & & & \mathbf{0}_{3\times3} & & \end{bmatrix}, B = \begin{bmatrix} 4.26 & 0 & 19.43 & 0.59 & 0.01 & -0.92 \\ 0 & 4.17 & 0 & -0.02 & 0.68 & 0 \\ -58.88 & 0 & 0.25 & 0.23 & 0.02 & 6.31 \\ 0 & 92.93 & -5.76 & -0.24 & 5.45 & -0.03 \\ -101.91 & 0 & 0 & -0.78 & 0 & 5.59 \\ 0 & 1.64 & -0.42 & 0 & -0.53 & 0 \\ \mathbf{0}_{3\times3} & & & \mathbf{0}_{3\times3} & & \end{bmatrix} \ (44)$$

$$C = I_{9\times9}.$$

4.2.4 System poles

The calculated frequencies of dutch-roll (3.83 rad/s) and short period (7.92 rad/s) modes in Tables 10 and 11 and Fig. 12 indicate good consistency with the natural frequency range of 1–10 rad/s estimated by Trondstad [36]. The identified roll mode is slightly faster than Trondstad's estimate, while the identified poles related to the phugoid and spiral divergence modes have periods of 0.99 rad/s and 0.42 rad/s, respectively, which are quite slow and were not

well captured by the system identification maneuvers in Table 3. For this reason, the exact placement of the phugoid and spiral divergence poles is less certain compared to the poles of the other modes. Nonetheless, the magnitude and relative placement of the identified poles are similar to those identified for the same type of aircraft in [25, 26, 28].

Having a pole-zero map makes it easy to assess the stability qualities of the system. The simplest stability analysis is performed by checking that all poles have negative real components. A more sophisticated analysis can be performed by analyzing the aerodynamic stability coefficients. For longitudinal static stability, the main requirement is a restoring pitching moment $C_{m\alpha} < 0$, while for lateral stability, the weathercock behavior is provided by a positive $C_{n\beta}$ and a stable dihedral effect which causes the vehicle to roll away from the sideslip [41, Chap. 3.1 and 3.4] is given by a negative $C_{l\beta}$. Thus, according to the coefficients in Table 8 and the poles in Fig. 12, the identified model is statically stable.

4.2.5 Linearized model prediction results

Figures 13 and 14 compare the model prediction results of the nonlinear and linearized models with the flight data. The following coloring scheme is used to differentiate between the models: black—flight data, blue—nonlinear model, orange—coupled linear model, and green—decoupled linear model.

An overview of the time series data in Figs. 13 and 14 shows that in most cases, the nonlinear model provides noticeably better predictions compared to the coupled and decoupled linear models, although the linear models are capable of replicating the measured flight data quite well.
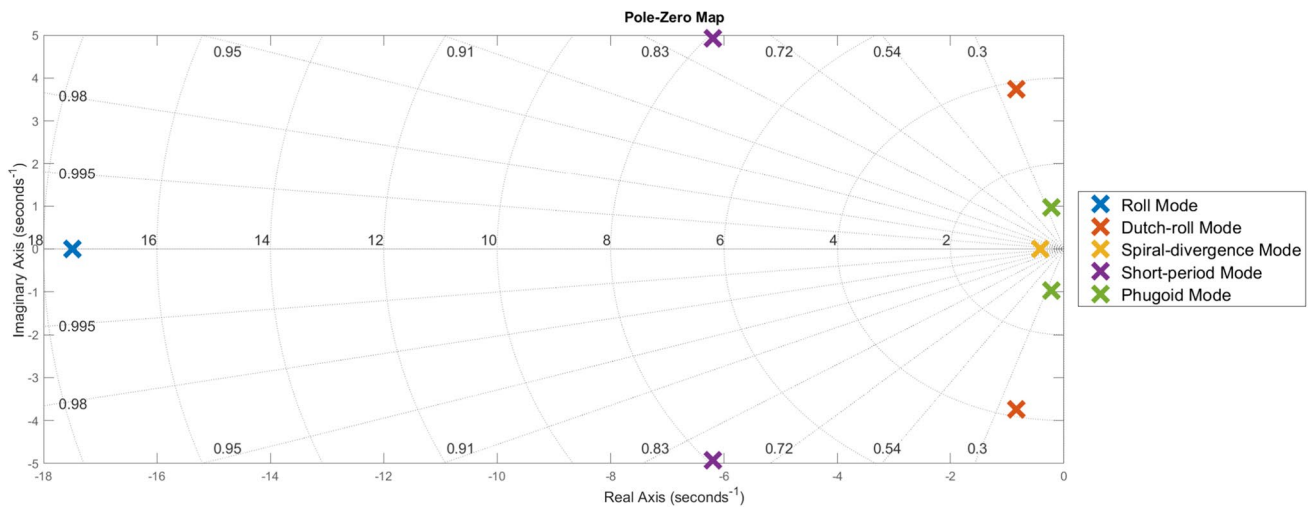
Fig. 12 System poles trimmed at $[V_a, \alpha, \beta] = [17.9\,m/s, 7.9°, 1.2°]$

Furthermore, the degradation of the linear model predictions is expected due to the change of the trim condition about which the model is linearized. A repeated re-linearization of the model, similar to what is done in an EKF, would improve the prediction performance of the models.

A particularly interesting result can be seen in the prediction of the angle of attack by the decoupled linear model in Fig. 14. The linear model prediction for the angle of attack during a lateral doublet maneuver is completely wrong. Comparing this to the angle of attack predictions during a longitudinal maneuver in Fig. 13, we can conclude that the angle of attack dynamics is influenced by more than just the longitudinal states of the aircraft and that analyzing 6-DOF dynamics with two decoupled linear models is not a good idea in the case of Skywalker X8 UAV.
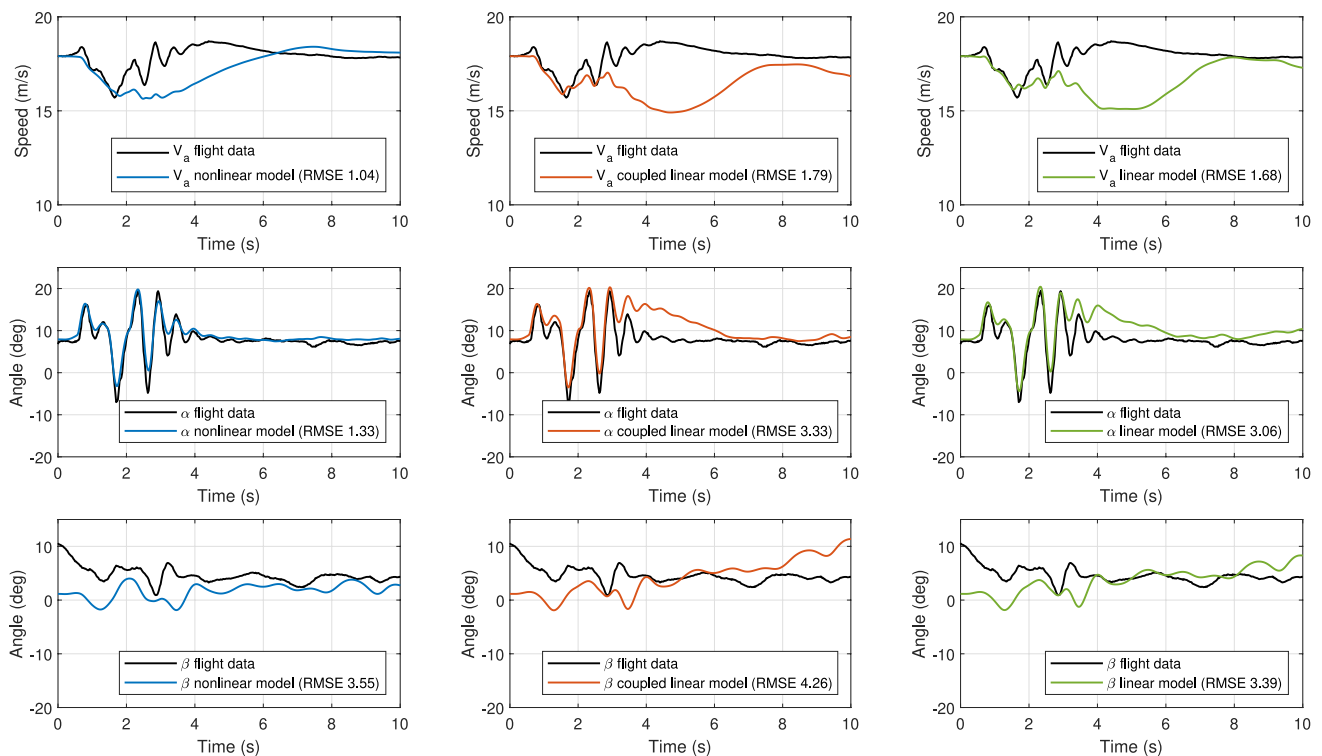
Fig. 13 Model predictions for a longitudinal *3-2-1-1* maneuver. RMSE is computed w.r.t. flight data in black
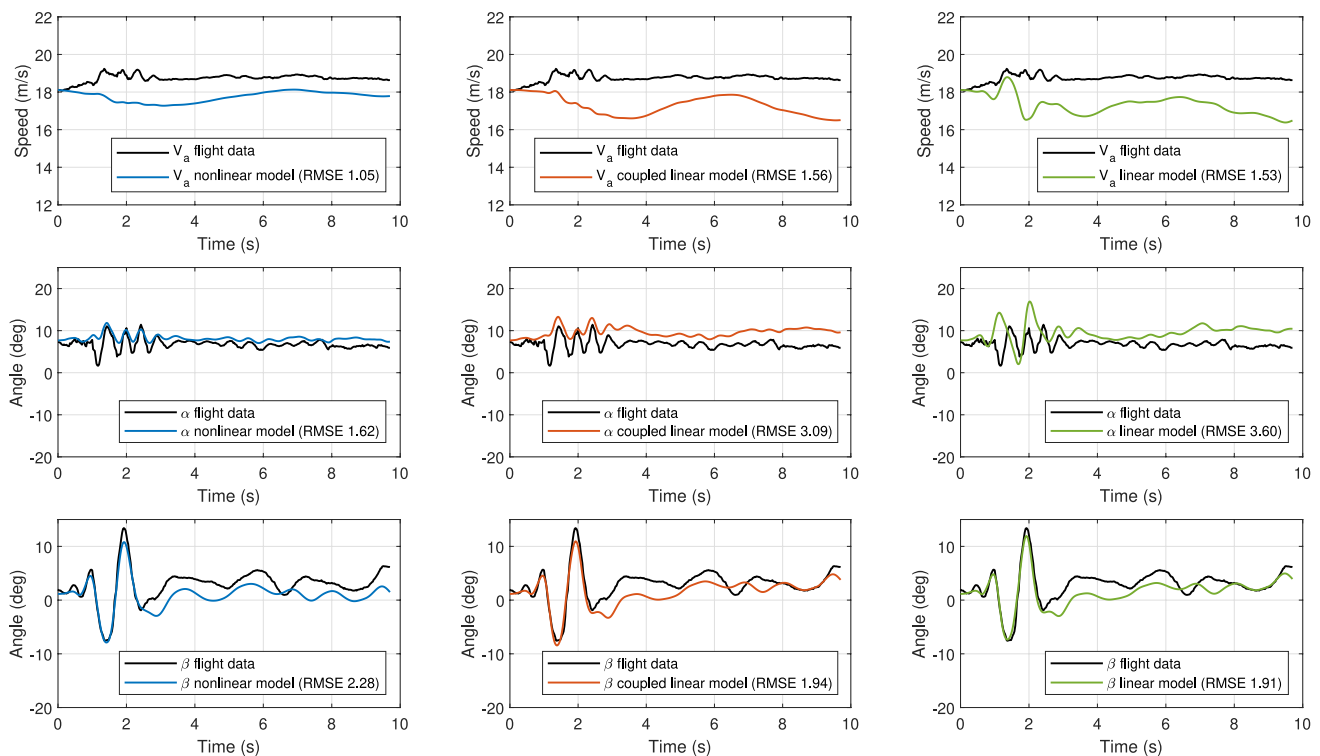
Fig. 14 Model predictions for a lateral *1-2-1* maneuver. RMSE is computed w.r.t. flight data in black

5 Conclusion

This paper addresses the need for accurate models to enable simulation-based testing and rapid development of applications tailored to small fixed-wing UAVs. While several small fixed-wing UAV models exist, as summarized in Table 2, few are parameterized in the stability frame, which is preferred in certain intra-disciplinary fields such as aircraft icing. Throughout this paper, we detailed the process of developing a simulation-ready nonlinear aerodynamic model of the Skywalker X8 platform, including its propulsion system and control surface actuators. We validated both the nonlinear and linearized models using flight data, demonstrating good agreement with the measured data during large dynamic maneuvers. However, we note that predictions near the steady state are less accurate due to estimation uncertainties and measurement noise. Finally, we presented a model assessment, including a pole-zero map and static stability properties of the identified model, facilitating easier comparison with other UAV modeling results.

This paper has examined several critical factors that influence the identification of small fixed-wing UAV models. Here, we revisit these key insights and challenges:

(1) The hybrid OEM: The nonlinear model presented in this article was identified using the hybrid OEM, where constructed force and moment coefficients are used as weighted outputs in addition to the directly measured data. In our study, the classical OEM did not work due to slow parameter convergence. Thus, the use of the force and moment coefficients as weighted outputs was critical to obtaining a good model.

(2) Wind susceptibility: Small, lightweight UAVs are highly sensitive to wind disturbances. Unlike larger aircraft, which act as low-pass filters for wind disturbances, the smaller platforms are affected significantly by wind gusts, making the model identification process challenging. It is, therefore, important to ensure that the flight experiments are performed in calm wind conditions. Moreover, direct measurement of the air data should be considered.

(3) Drag model: Modeling the aerodynamic drag remains challenging due to the aero-propulsive coupling. A way to decouple these effects is by performing specific maneuvers, e.g., a gliding maneuver where the motor can be turned off. Alternatively, a coupled aero-propulsive model can be identified [24]. In this article, the drag model uncertainty is partially mitigated by identifying an accurate propulsion system model based on wind tunnel experiments. Moreover, when motor speed measurements are not available, using all the relevant propulsion system measurements, including the battery voltage, can help improve the drag model. Finally, a thorough data pre-processing and removal of outliers is necessary when the measured data are noisy or are significantly affected by disturbances.

(4) Modeling assumptions: The lateral–longitudinal dynamics are decoupled in the identified nonlinear model. The decoupling choice was based on stepwise regression results and a simplification assumption, the validity of which was affirmed based on the model prediction results. However, since the model prediction results are imperfect, some prediction errors may be attributed to the unmodelled coupling effects.

(5) Region of validity: Aircraft dynamics are highly nonlinear; this means that the accuracy of a model identified at a specific trim point will deteriorate quickly for states far away from the trim. This has to do with Reynolds number, turbulence, and flow separation. In this paper, a decrease in model accuracy can be observed for negative α values, where there are only a few data points and the modeled lift and drag begin to deviate from the measurements.

5.1 Impact and future work

Our primary motivation for obtaining an aerodynamic model was to facilitate the development of GNC and fault monitoring algorithms essential for the operation of small fixed-wing UAVs in adverse weather conditions. We believe that our model provides a good representation of nominal Skywalker X8 UAV flight dynamics, thereby offering a solid foundation for the development of such algorithms.

In the specific case of UAV-icing, the obtained model will be integrated with icing-CFD results [12] and icing wind tunnel data [32, 33] to conduct realistic simulations of inadvertent icing encounters. The parameterization of the model in the stability frame will simplify the adaptation of ice-related penalties to changes in drag and lift coefficients, thereby improving the accuracy and reliability of the results.

While the model is useful as presented, it has certain limitations. In particular, the model lacks the description of the stall angle, and as discussed in Sect. 4.2.4, the slow mode dynamics were not well excited during the system identification maneuvers, resulting in a larger uncertainty associated with the identified spiral divergence mode. Furthermore, the chosen model structure decouples the lateral and longitudinal dynamics, making it less suitable for studying the interaction between drag, side force, and sideslip angle, which may be relevant for certain GNC algorithms. These are some of the limitations that can be investigated in future modeling efforts.

Data availability The flight experiment data that supports the findings of this study is publicly available in the repository [42].

Declarations

References

1. Federal Aviation Administration.: FAA Aerospace Forecast FY 2023-2043. USA (2023). https://www.faa.gov/dataresearch/aviation/aerospaceforecasts/faa-aerospace-forecast-fy-2023-2043. Accessed 11 Aug 2023

2. Shakhatreh, H., Sawalmeh, A.H., Al-Fuqaha, A., Dou, Z., Almaita, E., Khalil, I., Othman, N.S., Khreishah, A., Guizani, M.: Unmanned aerial vehicles (uavs): a survey on civil applications and key research challenges. IEEE Access **7**, 48572–48634 (2019). https://doi.org/10.1109/ACCESS.2019.2909530

3. Gao, M., Hugenholtz, C.H., Fox, T.A., Kucharczyk, M., Barchyn, T.E., Nesbit, P.R.: Weather constraints on global drone flyability. Sci. Rep. (2021). https://doi.org/10.1038/s41598-021-91325-w

4. Hann, R., Johansen, T.A.: Unsettled topics in unmanned aerial vehicle icing. Technical report, SAE Technical Paper (2020). https://doi.org/10.4271/EPR2020008

5. Deiler, C., Sachs, F.: Design and testing of an indirect ice detection methodology. Technical report, SAE Technical Paper (2023). https://doi.org/10.4271/2023-01-1493

6. Løw-Hansen, B., Hann, R., Stovner, B.N., Johansen, T.A.: Uav icing: a survey of recent developments in ice detection methods. IFAC-PapersOnLine **56**(2), 10727–10739 (2023). https://doi.org/10.1016/j.ifacol.2023.10.733

7. Hognadottir, S., Gryte, K., Hann, R., Johansen, T.A.: Inner-loop control of fixed-wing unmanned aerial vehicles in icing conditions. In: AIAA Scitech 2023 Forum (2023). https://doi.org/10.2514/6.2023-1049

8. Gryte, K., Hann, R., Alam, M., Roháč, J., Johansen, T.A., Fossen, T.I.: Aerodynamic modeling of the skywalker x8 fixed-wing unmanned aerial vehicle. In: 2018 International Conference on Unmanned Aircraft Systems (ICUAS), pp. 826–835 (2018). https://doi.org/10.1109/icuas.2018.8453370

9. Reinhardt, D., Gryte, K., Johansen, T.A.: Modeling of the skywalker x8 fixed-wing uav: Flight tests and system identification. In: 2022 International Conference on Unmanned Aircraft Systems (ICUAS), pp. 506–515 (2022). https://doi.org/10.1109/icuas54217.2022.9836104

10. Morelli, E.A., Klein, V.: Aircraft System Identification: Theory and Practice, 2nd edn. Sunflyte Enterprises, Williamsburg (2016)

11. Jategaonkar, R.V.: Flight Vehicle System Identification: A Time Domain Methodology, 2nd edn. AIAA, Reston (2015). https://doi.org/10.2514/4.102790

12. Lindner, M., Wallisch, J., Hann, R.: Uav icing: Numerical simulation of icing effects on wing and empennage. Technical report, SAE Technical Paper (2023). https://doi.org/10.4271/2023-01-1384

13. Hann, R., Hearst, R.J., Sætran, L.R., Bracchi, T.: Experimental and numerical icing penalties of an s826 airfoil at low reynolds numbers. Aerospace (2020). https://doi.org/10.3390/aerospace7040046

14. Fajt, N., Hann, R., Lutz, T.: The influence of meteorological conditions on the icing performance penalties on a uav airfoil. In: 8th European Conference for Aeronautics and Space Sciences (EUCASS) (2019). https://doi.org/10.13009/EUCASS2019-240

15. Deiler, C.: Aerodynamic modeling, system identification, and analysis of iced aircraft configurations. J. Aircr. **55**(1), 145–161 (2018). https://doi.org/10.2514/1.C034390

16. Deiler, C., Ohme, P., Raab, C., Mendonca, C., Silva, D.: Facing the challenges of supercooled large droplet icing: Results of a flight test based joint dlr-embraer research project. SAE Int. J. Adv. Curr. Pract. Mobil. **2**, 192–204 (2019). https://doi.org/10.4271/2019-01-1988

17. Deiler, C.: Comparison of flight characteristics of two different airplanes and ice configurations. J. Aircr. **57**(5), 995–1000 (2020). https://doi.org/10.2514/1.C035801

18. Deiler, C.: Flight characteristics with different supercooled large droplet ice configurations. Aeronaut. J. **126**(1299), 848–865 (2022). https://doi.org/10.1017/aer.2021.98

19. Deiler, C., Mönnich, W., Seher-Weiß, S., Wartmann, J.: Retrospective and recent examples of aircraft and rotorcraft system identification at dlr. J. Aircr. (2023). https://doi.org/10.2514/1.C037262

20. Arifianto, O., Farhood, M.: Development and modeling of a low-cost unmanned aerial vehicle research platform. J. Intell. Robot. Syst. **80**, 139–164 (2015). https://doi.org/10.1007/s10846-014-0145-3

21. Grymin, D.J., Farhood, M.: Two-step system identification and trajectory tracking control of a small fixed-wing uav. J. Intell. Robot. Syst. **83**, 105–131 (2016). https://doi.org/10.1007/s10846-015-0298-8

22. Lu, H.H., Rogers, C.T., Goecks, V.G., Valasek, J.: Online near real-time system identification on a fixed-wing small unmanned air vehicle. In: AIAA Atmospheric Flight Mechanics Conference, 2018 (2018). https://doi.org/10.2514/6.2018-0295

23. Simmons, B.M., McClelland, H.G., Woolsey, C.A.: Nonlinear model identification methodology for small, fixed-wing, unmanned aircraft. J. Aircr. **56**(3), 1056–1067 (2019). https://doi.org/10.2514/1.C035160

24. Simmons, B.M., Gresham, J.L., Woolsey, C.A.: Flight-test system identification techniques and applications for small, low-cost, fixed-wing aircraft. J. Aircr. (2023). https://doi.org/10.2514/1.C037260

25. Dorobantu, A., Murch, A., Mettler, B., Balas, G.: System identification for small, low-cost, fixed-wing unmanned aircraft. J. Aircr. **50**(4), 1117–1130 (2013). https://doi.org/10.2514/1.C032065

26. Venkataraman, R., Seiler, P.: System identification for a small, rudderless, fixed-wing unmanned aircraft. J. Aircr. **56**(3), 1126–1134 (2019). https://doi.org/10.2514/1.C035141

27. Matt, J.J., Hagerott, S.G., Svoboda, B.C., Flanagan, H.P., Chao, H.: Frequency domain system identification of a small flying-wing uas. AIAA Science and Technology Forum and Exposition, AIAA SciTech Forum 2022 (2022). https://doi.org/10.2514/6.2022-2407

28. Matt, J., Chao, H., Shawon, M.H., Hagerott, S.G.: Longitudinal system identification for a small flying-wing uas. In: AIAA SciTech Forum 2023 (2023). https://doi.org/10.2514/6.2023-0628

29. Valasek, J., Chen, W.: Observer/kalman filter identification for online system identification of aircraft. J. Guid. Control Dyn. **26**(2), 347–353 (2003). https://doi.org/10.2514/2.5052

30. Fossen, T.I.: Handbook of Marine Craft Hydrodynamics and Motion Control, 2nd edn. Wiley, Hoboken (2021)

31. Beard, R.W., McLain, T.W.: Small Unmanned Aircraft: Theory and Practice. Princeton University Press, Princeton (2012)

32. Løw-Hansen, B., Müller, N.C., Coates, E.M., Johansen, T.A., Hann, R.: Identification of an electric uav propulsion system in icing conditions. Technical report, SAE Technical Paper (2023). https://doi.org/10.4271/2023-01-1378

33. Coates, E.M., Wenz, A., Gryte, K., Johansen, T.A.: Propulsion system modeling for small fixed-wing uavs. In: 2019 International Conference on Unmanned Aircraft Systems (ICUAS), pp. 748–757 (2019). https://doi.org/10.1109/icuas.2019.8798082

34. Simmons, B.M.: System identification for propellers at high incidence angles. J. Aircr. **58**(6), 1336–1350 (2021). https://doi.org/10.2514/1.C036329

35. Özger, E.: Introducing a combined equation/output error approach in parameter estimation. 48th AIAA Aerospace Sciences Meeting Including the New Horizons Forum and Aerospace Exposition (2010). https://doi.org/10.2514/6.2010-34

36. Tronstad, P.L.: Model-based in-flight icing detection for fixed-wing uavs. Master's thesis, NTNU (2023). Accessed June 2, 2023. https://ntnuopen.ntnu.no/ntnu-xmlui/handle/11250/3100357

37. Bużantowicz, W.: Matlab script for 3d visualization of missile and air target trajectories. Int. J. Comput. Inf. Technol. **5**, 419–422 (2016)

38. Coates, E.M., Reinhardt, D., Gryte, K., Johansen, T.A.: Toward nonlinear flight control for fixed-wing uavs: system architecture, field experiments, and lessons learned. 2022 International Conference on Unmanned Aircraft Systems (ICUAS), pp. 724–734 (2022). https://doi.org/10.1109/icuas54217.2022.9836064

39. Borup, K.T., Fossen, T.I., Johansen, T.A.: A machine learning approach for estimating air data parameters of small fixed-wing uavs using distributed pressure sensors. IEEE Trans. Aerosp. Electron. Syst. **56**(3), 2157–2173 (2019). https://doi.org/10.1109/TAES.2019.2945383

40. Qiu, K.: ZoomPlot. GitHub release (2024). https://github.com/iqiukp/ZoomPlot-MATLAB/releases/tag/v1.5.1. Accessed 1 Feb 2024

41. Cook, M.V.: Flight Dynamics Principles A Linear Systems Approach to Aircraft Stability and Control, 3rd edn. Butterworth-Heinemann, Waltham (2013). https://doi.org/10.1016/c2010-0-65889-5

42. System identification campaign - Skywalker X8 UAV. DataverseNO, 1.0, https://doi.org/10.18710/U4TLYV (2024)